



*Facultad  
de  
Ciencias*

# **DINÁMICA DE SUPERFICIES FUERA DEL EQUILIBRIO**

(Surface dynamics out of equilibrium)

Trabajo de Fin de Grado  
para acceder al

**GRADO EN FÍSICA**

Autor: Jorge Martín Álvarez

Director: Juan Manuel López Martín

Co-director: Enrique Rodríguez Fernández

Junio 2023



## Agradecimientos

Con este trabajo se cierra el lustro que he pasado como estudiante de Física en la Universidad de Cantabria. Supe que quería ser físico cuando participé y disfruté de las Olimpiadas de Física en el último año instituto, y estoy orgulloso de haber cumplido ese deseo cinco años después, sin haber dejado de lado el resto de pasiones de mi vida.

En primer lugar, quiero agradecer a mi director, Juanma, la ayuda insustituible durante los últimos meses, así como el haberme propuesto como trabajo un tema actual de investigación con el que he aprendido tanto. Igualmente agradezco a mi codirector, Enrique, la implicación que ha tenido permanentemente, resolviendo mis numerosas dudas y dándome valiosos consejos. Sin las aportaciones de ambos, estoy convencido de que la calidad de este trabajo sería muy inferior.

Debo señalar, además, que este trabajo forma parte del proyecto que realizo junto con el Prof. Juan Manuel López en el Instituto de Física de Cantabria del CSIC como beneficiario de una beca de introducción a la investigación JAE Intro 2022 otorgada por el Ministerio de Ciencia e Innovación.

Asimismo, doy las gracias también a todos los profesores de física que he tenido durante el grado, tanto en Santander como en Innsbruck, con especial afecto para Ángel, Ignacio y José Ángel, por haberme transmitido tanto conocimiento en campos variados de esta disciplina.

A mis padres, por iniciarme en esta materia en el instituto y seguir ahí siempre, y al resto de mi familia, entre otras cosas por hacerme tan feliz en Liendo y Villaprovedo.

A Alejandro y Joseba, por comprarme batidos de chocolate, y al resto de doblegradistas, por tantas horas juntos en esta aventura; también a Pablo, por irse al lado oscuro. A Blanca y José Ángel por su confianza y comunicación, y a Manu y Pablo por todas las anécdotas y frases olímpicas que nunca olvidaremos. Y por último, a todas las personas que se cruzaron en mi camino entre Bratislava, París e Innsbruck.

# Resumen

En la dinámica de superficies fuera del equilibrio, la ecuación de Kardar-Parisi-Zhang (KPZ) destaca como el modelo no lineal más simple que presenta soluciones invariantes de escala. En este trabajo realizamos un estudio numérico de esta teoría mediante la ecuación de Burgers estocástica en una dimensión, que se puede obtener como la derivada espacial de la ecuación de KPZ. De este modo, calculamos el campo solución de la ecuación de Burgers y posteriormente obtenemos su primitiva, que es una solución de KPZ. En la primera parte, se integra la ecuación de Burgers determinista con el fin de verificar el esquema numérico empleado. A continuación, consideramos la ecuación de Burgers estocástica con ruido no correlacionado, obteniendo resultados compatibles con los estudios analíticos y numéricos previos. Finalmente, analizamos el efecto de incluir correlaciones temporales en el término de ruido. Los resultados sugieren la existencia de un índice de correlación umbral, por debajo del cual el comportamiento del sistema es próximo al caso no correlacionado. Por otro lado, detectamos escalamiento anómalo intrínseco por encima de un índice umbral diferente. El código completo empleado en la integración numérica es de elaboración propia.

**Palabras clave:** dinámica de superficies, ecuación de KPZ, ecuación de Burgers estocástica, ruido con correlaciones temporales.

# Abstract

The Kardar-Parisi-Zhang (KPZ) equation stands out in kinetic roughening as the simplest non-linear, out-of-equilibrium model exhibiting scale-invariant solutions. In this work, we conduct a numerical study of the dynamics of surfaces out of equilibrium by means of the one-dimensional stochastic Burgers equation, which can be obtained as the spatial derivative of the KPZ equation. Like this, we compute the time evolution of the solution field of the Burgers equation and then get its primitive field as a solution of KPZ. In the first part we integrate the deterministic Burgers equation in order to check our numerical scheme. Next, we consider the stochastic Burgers equation with uncorrelated noise, obtaining results compatible with previous analytical and numerical studies. In the end, we investigate the effects of long term temporal correlations in the noise term. Our results suggest the existence of a threshold correlation index below which the behaviour of the system is not too different from the uncorrelated case. In turn, we observe the emergence of intrinsic anomalous scaling above another threshold index. The computing code used in the numerical integration is entirely self-developed.

**Key words:** kinetic roughening, KPZ equation, stochastic Burgers equation, temporally correlated noise.

# Contents

<b>Introduction</b>	<b>1</b>
<b>1 Surface growth processes</b>	<b>3</b>
1.1 Observables in surface growth . . . . .	4
1.2 Kinetic roughening . . . . .	5
1.2.1 Anomalous scaling . . . . .	7
1.2.2 Linear models . . . . .	8
1.2.3 Non-linear models . . . . .	9
1.3 Numerical methods . . . . .	10
1.3.1 Integration scheme for the Burgers equation . . . . .	11
1.3.2 Generation of long-time correlated noise . . . . .	11
<b>2 The deterministic Burgers equation</b>	<b>14</b>
2.1 An exact solution: the Cole-Hopf transformation . . . . .	14
2.2 The inviscid equation . . . . .	15
2.2.1 Method of characteristics . . . . .	16
2.3 The general form: viscous Burgers equation . . . . .	18
2.4 Numerical integration of the deterministic equation . . . . .	18
<b>3 The stochastic Burgers equation with white noise</b>	<b>24</b>
3.1 The multiple regimes of a KPZ system . . . . .	25
3.2 Existing analytical results . . . . .	25
3.2.1 Random deposition . . . . .	25
3.2.2 Edwards-Wilkinson equation . . . . .	26
3.2.3 KPZ equation . . . . .	26
3.3 Numerical integration of the stochastic equation with uncorrelated noise	28
<b>4 The stochastic Burgers equation with correlated noise</b>	<b>36</b>
4.1 Existing results on long range temporal correlations . . . . .	37
4.1.1 Edwards-Wilkinson equation with correlated noise . . . . .	37
4.1.2 KPZ equation with columnar noise . . . . .	38
4.1.3 KPZ equation with correlated noise . . . . .	38
4.2 Numerical integration of the stochastic equation with correlated noise .	39
<b>5 Conclusions</b>	<b>45</b>
<b>References</b>	<b>47</b>



# Introduction

In a three-dimensional universe like the one we inhabit, surfaces are present all round as the boundaries separating two objects in contact. For instance, the earth's (continental) surface is the interface between the crust and the atmosphere, the skin sets the boundaries of our body and the event horizon delimits the borders of a black hole. In this way, many subjects of interest in diverse fields of science are closely linked to surfaces, such as friction forces in physics, aerodynamic devices in engineering, cell membranes in biology or a whole set of problems in mathematics, to cite some of them. In most cases, the morphology of the surface is a crucial aspect of the study, as it determines the effects and properties observed, and therefore the study of surfaces on their own emerges as a relevant topic with uncountable applications in other areas.

As is the case with most of the aforementioned interfaces, surfaces are usually present in nature and develop in time subject to different laws, which can be due to multiple processes. Subsequently, we are not only keen on the morphology of a surface at a given time, but also on its dynamics. The analysis of the formation and later evolution of an interface and its morphology is frequently known as the study of the *surface growth* [4]. The study of interfaces can be extended to other dimensions, given that the observables that we shall use are not restricted to two-dimensional surfaces. Like this, a complete theory about interface dynamics in any dimension can be deduced by carrying out a generalization of the phenomena observed in two dimensions.

The modelling of surface dynamics is generally carried out by means of stochastic differential equations containing a noise term which accounts for the random factors in the growth process. One specific instance of surface growth is *kinetic roughening*, which characterizes systems presenting totally disordered interfaces in the long term that exhibit scale invariant properties. Typically, the disorder in surfaces subject to kinetic roughening processes grows until reaching a stationary saturation regime. The growth rate and the point of saturation are determined by the so-called *critical exponents*, which are generally used to define *universality classes*. In this way, systems with apparently different features which show the same behaviour in terms of the critical exponents are grouped in the same class.

Among the mathematical models aiming to describe kinetic roughening, the Kardar-Parisi-Zhang (KPZ) equation emerges as one of the most prominent. This non-linear stochastic differential equation was first proposed by M. Kardar, G. Parisi and Y.-C. Zhang in 1986 [20] seeking a better description of kinetic roughening processes than previous attempts. These included two basic models that had successfully explained some features observed in kinetic roughening: random deposition and the linear Edwards-Wilkinson equation [12]. While these equations failed to describe the long term behaviour of certain processes later characterized by the KPZ model, they play a relevant role in the evolution of KPZ systems as they rule transitory regimes.

Interestingly, the importance of the KPZ equation does not rely only on the accurate description of surface growth processes that it provides, but also in the wide-ranging amount of problems in non-equilibrium physics that lie within its universality class. Some examples of these are directed polymers in random media, turbulent liquid crystals, bacterial range expansion or the asymmetric simple exclusion process and its variations. For this reason, remarkable efforts have been put in the study of the

KPZ equation over the last 40 years, leading to significant analytical and numerical results. In particular, its connection with the theory of random matrices has been analysed, leading to identifying the fluctuations statistics of the KPZ systems with the Tracy-Widom distribution. Subsequently, an exact solution was found in the late 2000s independently in mathematics by G. Amir, I. Corwin and J. Quastel [3] and mathematical physics by T. Sasamoto and H. Spohn [34], employing (unsurprisingly) similar approaches [10].

Another system in the KPZ universality class is related to stochastic hydrodynamics. Indeed, taking the spatial derivative of the KPZ equation results in the stochastic Burgers equation, the noisy version of the deterministic Burgers equation that models fluids as a simplified instance of the Navier-Stokes equation. Specifically, the stochastic Burgers equation describes the evolution of the velocity field of a randomly stirred fluid. Our goal in this work is the numerical study of the one-dimensional stochastic Burgers equation as an approach to the analysis of kinetic roughening processes. We will simulate a discretized version of the Burgers equation to obtain the time evolution of velocity field, and then compute its primitive field that should be a solution of the corresponding KPZ equation.

The work is divided in four chapters. In Chapter 1, we set the formalism used in kinetic roughening processes. We define the main observables that shall characterize the systems throughout the work and present the most relevant models, including the three mentioned above. We also detail the numerical scheme used for the integration of the Burgers equation and the algorithm for generating temporally correlated noise in Chapter 4.

Chapter 2 is dedicated to the study of the deterministic Burgers equation, which models fluids with no external force. In addition to its intrinsic interest, the deterministic equation will allow us to check our numerical method and understand the influence of each of the terms in the resulting solution. We introduce the Cole-Hopf transformation, which leads to obtaining an exact solution, and review the method of characteristics, which allows to describe the solutions in the inviscid case. In the end, we simulate the deterministic equation, focusing on observing its characteristic features and measuring the magnitudes that will be relevant in the stochastic equation.

In Chapter 3 we study the stochastic Burgers equation with conserved, uncorrelated noise, which is the spatial derivative of the KPZ equation. We start by reviewing existing analytical results in the random deposition, Edwards-Wilkinson and KPZ models, as we expect the three regimes are expected to be observed in the time evolution of KPZ systems. We then show the results of the numerical integration of the stochastic Burgers equation and compare the critical exponents measured in the Burgers velocity field and the primitive KPZ height field with previously published results.

Finally, in Chapter 4 we analyse the effects of long-term temporal correlations in the noise term of the stochastic Burgers equation. The study of temporal correlations is motivated as real physical systems generally show correlations to some extent, while some present strong correlations leading to notably different properties. Again, we outline the most relevant published results and then present the outcome of our simulations, which focus on determining the dependence of the critical exponents on the correlation strength with the aim of obtaining a new set of results that can be compared to the unclear existing literature on the topic.

# 1 Surface growth processes

The formation of interfaces is generally ruled by multiple factors, most of them at microscopic scales, making unfeasible the attempt to provide a complete description of the details of these processes. Conversely, as is the case in many other fields in physics, the theory of surface growth focuses on finding a small number of basic laws which are sufficient to describe the global behaviour of an interface. We dedicate this chapter to set the fundamental concepts in surface dynamics, define the observables that we shall use to analyse interfaces and review the most relevant models aiming to characterize growth processes. Even though we will restrict to one-dimensional interfaces in the rest of the work, we carry out this general introduction in arbitrary dimension, given that the generalization is straightforward.

In order to illustrate surface growth problems, let us present a couple of examples showing that surface growth problems are more common than we imagine in our everyday life. When spilling a liquid over the tablecloth, the evolution of the (one-dimensional) interface separating the wet and dry parts is a form of surface growth. Essentially the same process is observed when a sheet of paper is slowly burnt from one of its ends. Other natural occurrences, like propagation of flame fronts or flux lines in a superconductor, admit a parallel description, even though they present different size scales, showing a *universal* behaviour. This is actually a very common feature in this kind of problems: we can classify processes into *universality classes*, in such a way that the same equation (up to a possible *rescaling* change of variables) describes very different systems in nature. We will see this in detail when we introduce some of the models often used for surface growth.



Figure 1.1: Typical interface created by the accumulation of snowflakes on a window.

Another typical set of surface growth phenomena is that of deposition processes: starting from a flat interface, we let particles fall on a random position and stick to the particles deposited previously. Snowflakes collecting on a slanted glass window is an example of this process. The random deposition of the particles makes the surface grow towards a *rough* interface, as Fig. 1.1 depicts. Similar shapes are observed when atoms are deposited on top of a clean surface forming thin films by molecular beam epitaxy (MBE).

## 1.1 Observables in surface growth

In general, surface growth processes are not deterministic, or at least not to our eyes. Even though the snowflakes deposition or the advance of the liquid on the tablecloth follow deterministic equations, their details (i.e. fast internal degrees of freedom) are by far inaccessible to us and we perceive them as random processes. Therefore, statistical observables are used in order to study the surface dynamics of interfaces and classify systems showing a common evolution of these observables.

On this matter, we consider an evolving interface given by a function  $h(\mathbf{x}, t)$ , defined over a spatial  $d$ -dimensional domain  $\Omega = [0, L]^d$  for a positive real number  $L$ , called the lateral size of the system. In these conditions, we present the observables that we will use in our work [31]. Physical systems are normally defined in the continuum, but simulations need to be done on discrete, finite systems, so we also consider discrete definitions of the observables. The details on how to carry out the discretization are given in section 1.2.3. Moreover, given that we study stochastic processes, we will generally perform multiple noise realizations and focus on the average value of each observable, denoted by  $\langle \cdot \rangle$ .

- The *surface roughness* is the standard deviation of the height values of the surface at a given time,

$$W(t) = \left\langle \left( \frac{1}{L^d} \int_{\Omega} (h(\mathbf{x}, t) - \bar{h}(t))^2 d\mathbf{x} \right)^{1/2} \right\rangle. \quad (1.1)$$

In the expression above,  $\bar{h}(t)$  denotes the mean value of  $h$  over the domain  $\Omega$  at time  $t$ . For the discrete systems used in simulations,  $L$  is set to be an integer and the expression becomes

$$W(t) = \left\langle \left( \frac{1}{L^d} \sum_{i=1}^{L^d} (h(\mathbf{x}_i, t) - \bar{h}(t))^2 \right)^{1/2} \right\rangle. \quad (1.2)$$

The roughness is the most basic measure of the level of disorder.

- Two further statistical observables for measuring the disorder of a given configuration are *skewness* and *kurtosis*. Skewness measures the asymmetry of a distribution around its mean, and is defined as

$$\mathcal{S}(t) = \frac{1}{W^3(t)} \left\langle \frac{1}{L^d} \int_{\Omega} (h(\mathbf{x}, t) - \bar{h}(t))^3 d\mathbf{x} \right\rangle. \quad (1.3)$$

In turn, kurtosis measures how important the largest deviations from the mean (outliers) are. It is given by

$$\mathcal{K}(t) = \frac{1}{W^4(t)} \left\langle \frac{1}{L^d} \int_{\Omega} (h(\mathbf{x}, t) - \bar{h}(t))^4 d\mathbf{x} \right\rangle. \quad (1.4)$$

A Gaussian distribution verifies  $\mathcal{K} = 3$ , thus it is usual to consider the *excess kurtosis*  $\mathcal{K}_e := \mathcal{K} - 3$  when deciding whether a given distribution is Gaussian. The corresponding expressions for a discrete system of integer size  $L$  are analogous to the case of surface roughness.

- The *power spectral density* (PSD), also known as *height structure factor*, measures the contribution of each mode in the spatial Fourier spectrum. It is given by

$$S_h(\mathbf{k}, t) = \left\langle \hat{h}(\mathbf{k}, t) \hat{h}(-\mathbf{k}, t) \right\rangle = \left\langle |\hat{h}(\mathbf{k}, t)|^2 \right\rangle, \quad (1.5)$$

where  $\hat{h}(\mathbf{k}, t)$  is the Fourier transform of  $h(\mathbf{x}, t)$ , defined as

$$\hat{h}(\mathbf{k}, t) = \frac{1}{L^d} \int_{\Omega} h(\mathbf{x}, t) e^{-i\mathbf{k}\cdot\mathbf{x}} d\mathbf{x}. \quad (1.6)$$

Therefore, it allows to identify the dominant spatial scales in the system at a given time. It is related to the surface roughness as

$$W^2(t) = \sum_{\mathbf{k} \neq \mathbf{0}} S_h(\mathbf{k}, t). \quad (1.7)$$

## 1.2 Kinetic roughening

The morphology of interfaces in surface dynamics can present very different features depending on the characteristics of the effect causing the surface growth. A first distinction can be done between systems that evolve towards ordered patterns and those showing high spatio-temporal disorder in the long term. Our interest focuses on the systems that exhibit totally disordered interfaces. In this case, the behaviour of the surface does not depend on the spatial and temporal scales of the system. We will later characterize this phenomenon, known as *scale invariance*. The concept has its origin in the theory of phase transitions in statistical physics. A typical example is the ferromagnetic transitions described by the Ising model, where a typical size for the spin clusters cannot be found, resulting in fractal patterns in the spin field at the critical point [31].

The form of surface growth happening in systems which present scale invariance is called *kinetic roughening*. These processes show a common behaviour regarding the evolution of the statistical observables defined above. We now introduce the general theory of kinetic roughening and define relevant concepts that emerge from them, namely the so-called *critical exponents*. Furthermore, we list some of the models that better describe kinetic roughening, the so-called universality classes of surface growth.

Let us consider then a kinetic roughening process on a finite system of lateral size  $L$ , with a flat interface  $h(\mathbf{x}, 0) \equiv 0$  as initial condition. The evolution of the surface roughness for several sizes is depicted in Fig. 1.2. First, the roughness increases as a power of time until reaching a saturation value  $W_{\text{sat}}$ . Saturation takes place at a time  $t_{\text{sat}}$ , when correlations have spread to the whole system

$$W(t) \sim \begin{cases} t^\beta, & \text{if } t \ll t_{\text{sat}}; \\ W_{\text{sat}}, & \text{if } t \gg t_{\text{sat}}. \end{cases} \quad (1.8)$$

The exponent  $\beta$  is called *growth exponent*, and remains the same no matter the lateral size  $L$ . However, the saturation value  $W_{\text{sat}}$  does depend on  $L$ , and thus also  $t_{\text{sat}}$ , according to the expressions

$$W_{\text{sat}} \sim L^\alpha; \quad t_{\text{sat}} \sim L^z. \quad (1.9)$$

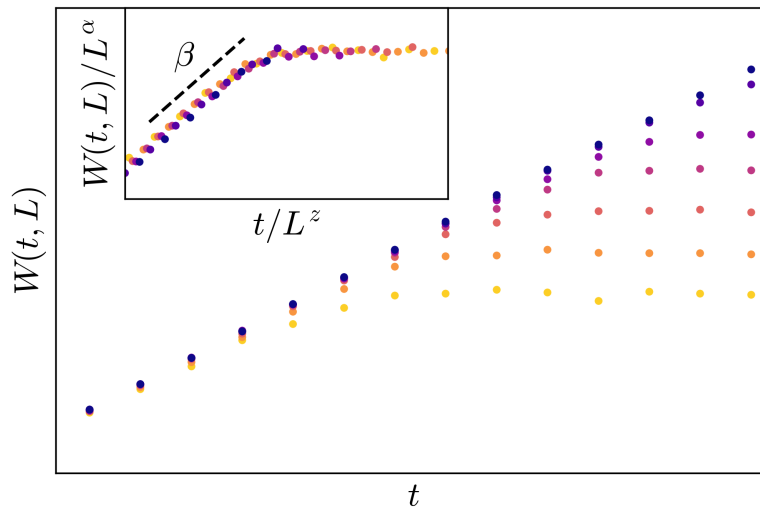


Figure 1.2: Evolution of the surface roughness for increasing lateral sizes in a kinetic roughening process. Yellow points correspond to the smallest size and blue to the largest. Data correspond to the one-dimensional KPZ height field and have been obtained by integrating the Burgers equation (3.3) as in Chapter 3. The inset shows the collapsed data using the corresponding scaling exponents  $\alpha = 1/2$  and  $z = 3/2$ .

The exponent  $\alpha$  is said to be the *roughness exponent*, while  $z$  is called the *dynamic exponent*. The relation  $\alpha = \beta z$  follows from the definitions. Moreover, the following relation between the roughness exponent and the fractal dimension  $D_f$  of the surface holds [25]:

$$\alpha = d + 1 - D_f. \quad (1.10)$$

With all that, a general expression for  $W(L, t)$  can be found:

$$W(L, t) \sim L^\alpha f_W \left( \frac{t}{L^z} \right), \quad (1.11)$$

where

$$f_W(u) \sim \begin{cases} u^\beta, & \text{if } u \ll 1; \\ 1, & \text{if } u \gg 1, \end{cases} \quad (1.12)$$

and a smooth transition in the region connecting the two limits. eq. (1.11) is called the Family-Vicsek scaling relation [14]. It follows that the evolution of the roughness in systems with different lateral size is the same, up to rescaling the variables  $h$  and  $t$ . The inset in Fig. 1.2 shows this behaviour, known as scale invariance.

Similarly, the height structure factor typically behaves as

$$S_h(\mathbf{k}, t) \sim \begin{cases} t^{(2\alpha+d)/z}, & \text{if } k^{-1} \ll t^{1/z}; \\ k^{-(2\alpha+d)}, & \text{if } k^{-1} \gg t^{1/z}, \end{cases} \quad (1.13)$$

where  $k := |\mathbf{k}|$  denotes the module of the wavenumber, and  $\alpha$  and  $z$  are the same as above. Again, we find the following scaling relation:

$$S_h(\mathbf{k}, t) \sim k^{-(2\alpha+d)} f_S(k^z t), \quad (1.14)$$

with

$$f_S(u) \sim \begin{cases} u^{(2\alpha+d)/z}, & \text{if } u \ll 1; \\ 1, & \text{if } u \gg 1. \end{cases} \quad (1.15)$$

Fig. 1.3 depicts the time evolution of  $S_h(\mathbf{k}, t)$  in a kinetic roughening process.

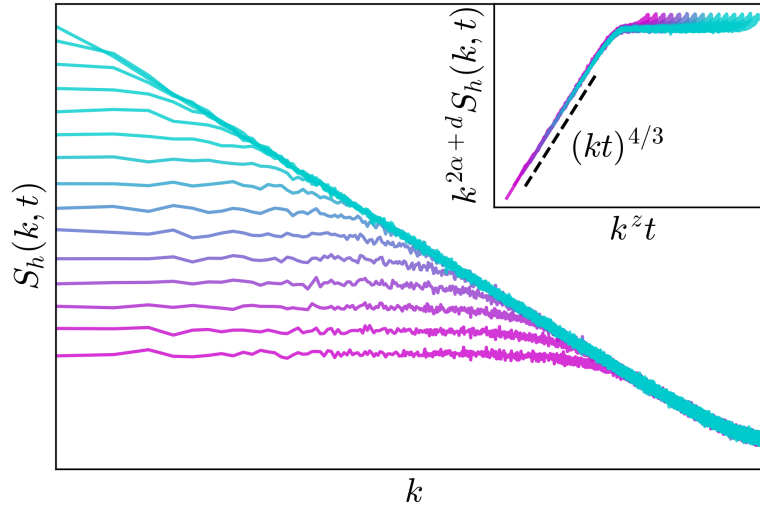


Figure 1.3: Time evolution of the PSD for the largest system of the ones in Fig. 1.2. Starting in the lowest curve (pink), time is gradually increased with a factor 2 until reaching  $t_{\text{sat}}$ . The insets shows the collapsed data for the corresponding scaling exponents  $\alpha = 1/2$  and  $z = 3/2$ .

Interestingly, the critical exponents do not depend on the specific details of the system, such as its viscosity or the intensity of the random process provoking kinetic roughening. Nonetheless, a single system can go through several regimes as different effects may dominate its evolution at different time scales. We will better discuss this behaviour once we present the most common models of kinetic roughening.

Other than the surface roughening and the height structure factor, surface growth processes are also characterized by the probability distribution of the fluctuations of the height field. In particular, measuring the evolution of the skewness and excess kurtosis of the field allows to distinguish between different distributions in some cases.

### 1.2.1 Anomalous scaling

Under certain conditions, however, the expressions above do not correctly describe kinetic roughening processes. Specifically, the *spectral* roughness exponent in eq. (1.13), that we shall henceforth denote as  $\alpha_s$ , may be different from the one defined in eq. (1.9). This is known as *intrinsic anomalous scaling* [30]. In this case, a slightly different mathematical description of the structure factor is necessary,

$$S_h(\mathbf{k}, t) \sim k^{-(2\alpha+d)} f_{S'}(k^z t), \quad (1.16)$$

where

$$f_{S'}(u) \sim \begin{cases} u^{(2\alpha+d)/z}, & \text{if } u \ll 1; \\ u^{2(\alpha-\alpha_s)}, & \text{if } u \gg 1. \end{cases} \quad (1.17)$$

One example of a system which exhibits anomalous scaling is the one that we study in Chapter 4, where the global and spectral roughness of the KPZ equation with temporally correlated noise differ above a certain threshold. Moreover, we will see that in this situation  $\alpha_s > 1$ . This leads to a splitting between the spectral exponent and the *local* exponent  $\alpha_{\text{loc}}$ , which is defined from the roughness evolution at different spatial scales and is bounded by 1 [31]. Hence, a different kind of anomalous scaling is found, known as *super-roughness* [30]. The combination of both effects leads to the formation of facets in the surface morphology, and we talk about faceted systems [1].

### 1.2.2 Linear models

A variety of mathematical models are used to describe with kinetic roughening problems, based on the distinct features and the relevant parameters of each system. The simplest ones are given by linear differential equations, and in these cases exact analytical results for the observables introduced above can be obtained. Here we give the details of two of them.

The most basic linear model reproducing kinetic roughening is a *random deposition* process, given by

$$\partial_t h = \eta(\mathbf{x}, t), \quad (1.18)$$

where  $\eta(\mathbf{x}, t)$  is an uncorrelated noise term verifying

$$\langle \eta(\mathbf{x}, t) \rangle = 0; \quad \langle \eta(\mathbf{x}_1, t_1) \eta(\mathbf{x}_2, t_2) \rangle = 2D \delta^d(\mathbf{x}_1 - \mathbf{x}_2, t_1 - t_2), \quad (1.19)$$

for a given noise intensity  $D$ . Such a noise function is usually referred to as *white* noise, given that there is no dominant frequency in either the time or space Fourier spectra. The behaviour of the critical exponents in random deposition processes is special, since the roughness scales as  $W(t) \propto t^{1/2}$  for any  $t > 0$ . In other words, as there is no mechanism leading to correlation along the interface, a saturation value is not achieved, which can be interpreted as  $\alpha$  and  $z$  being infinite.

The introduction of a relaxation term in eq. (1.18), which takes into account height diffusion in the surface and therefore produces smoother solutions, leads to the *Edwards-Wilkinson* (EW) model [12]:

$$\partial_t h = \nabla^2 h + \eta(\mathbf{x}, t). \quad (1.20)$$

When  $\eta$  is again a white noise, the critical exponents of the one-dimensional EW equation are  $z = 2$ ,  $\alpha = 1/2$  and  $\beta = \alpha/z = 1/4$ . As stated before, changing the relative strength of the terms in the equation does not alter the values of the exponents. In contrast, considering other correlation relations than the one in eq. (1.19) leads to a different set of critical exponents and also anomalous scaling, as we shall study in detail in Chapter 4.

Other linear models are given by a stochastic equation of the form

$$\partial_t h = -(-\nabla^2)^{z/2} h + \eta(\mathbf{x}, t), \quad (1.21)$$

which is a generalization of eq. (1.20) for arbitrary  $z$ . The scaling exponents for any of these equations and any dimension  $d$  can be obtained analytically, as shown in [31].

### 1.2.3 Non-linear models

Among the non-linear models, the *Kardar-Parisi-Zhang* (KPZ) equation stands out as the most relevant one. Originally conceived for describing the dynamics of surface growth [20], its relevance is also due to its multiple applications in non-equilibrium statistical physics. These include, for instance, the study of directed polymers in random media, particle transport, driven-dissipative Bose-Einstein condensates, the asymmetric simple exclusion process or bacterial range expansion [31, 35]. The KPZ equation reads

$$\partial_t h = \nu \nabla^2 h + \frac{\lambda}{2} (\nabla h)^2 + \eta(\mathbf{x}, t), \quad (1.22)$$

where the viscosity  $\nu \geq 0$  and coupling constant  $\lambda$  are parameters representing the strengths of diffusion and non-linearity, respectively, and  $\eta$  is an uncorrelated noise as in eq. (1.19). An equivalent formulation of eq. (1.22) is obtained by considering the gradient field  $\mathbf{u} = \nabla h$  of the height function and differentiating. This leads to

$$\partial_t \mathbf{u} = \nu \nabla^2 \mathbf{u} + \lambda (\mathbf{u} \nabla \mathbf{u}) + \nabla \eta(\mathbf{x}, t), \quad (1.23)$$

which bears the name of *Burgers* equation with conserved noise, since the noise term is now the derivative of the one in eq. (1.22). We dedicate Chapter 2 to the study of the Burgers equation without noise (or *deterministic* Burgers equation), which was initially derived as a simpler version of Navier-Stokes equation for fluids. The noise term models the effect of random stirring, adding random stirred fluids to the long list of phenomena described by the KPZ equation. Inversely, the Burgers equation provides an equivalent approach to the problems addressed by KPZ, with the possibility of checking the results given by the latter or exploring different numerical methods. The observables defined in eqs. (1.1) and (1.5) can be considered analogously for the velocity field, including the PSD  $S_u(\mathbf{k}, t)$  that we shall later refer to.

Eq. (1.22) depends on three parameters  $\nu$ ,  $\lambda$  and  $D$ , the latter being implicit in the correlation relation for  $\eta$ , but they are not independent. The following transformations into dimensionless variables

$$\bar{\mathbf{x}} = \frac{\mathbf{x}}{x_0}, \quad \bar{t} = \frac{t}{\nu^{-1} x_0^2}, \quad \bar{h} = \frac{h}{D^{1/2} \nu^{-1/2} x_0^{1/2}}, \quad (1.24)$$

for arbitrary  $x_0$ , transform eq. (1.22) into (dropping bars on variables)

$$\partial_t h = \nabla^2 h + \frac{\bar{\lambda}}{2} (\nabla h)^2 + \eta(\mathbf{x}, t), \quad (1.25)$$

where  $\bar{\lambda} = \lambda \left(\frac{D}{\nu^3} x_0\right)^{1/2}$  and  $\eta$  has now unit variance. The length  $x_0$  is fixed for a given system and can be set to 1 as the discretization step. This allows us to consider henceforward  $\nu = D = 1$ , and use  $\bar{\lambda} = \lambda \left(\frac{D}{\nu^3}\right)^{1/2}$  as the reference parameter of the KPZ equation. The transformation is not possible in the deterministic case though, so we will keep working with both parameters in Chapter 2.

As mentioned above, a system usually goes through different regimes before reaching a stationary state. Even in the KPZ model, linear regimes (random deposition first, EW afterwards) are typically dominant at small times, while non-linearity is

only observed after certain time. The time scales are influenced by the parameters of eq. (1.22), while the system size determines whether different regimes are reached before saturation. In particular, larger  $L$  and  $\lambda$  are convenient for observing non-linear effects. This behaviour is relevant in the analysis of our results in Chapters 3 and 4.

In such systems, an important observable to look at is the distribution of the height field. In the random deposition and EW models, the interface presents a Gaussian distribution at any time. In contrast, fluctuations in the growing non-linear regime in the KPZ equation follow the so-called *Tracy-Widom* (TW) distribution, before turning back to Gaussian after saturation [31]. The origin of the TW distribution is found in the theory of random matrices, as the probability distribution of the normalized largest eigenvalue of a random Hermitian matrix [37]. Fig. 1.4 compares both distributions. Among its properties, we remark that neither the skewness (since it is asymmetric) nor the excess kurtosis are zero, allowing to use these observables as an indicator of the dominant regime at each time.

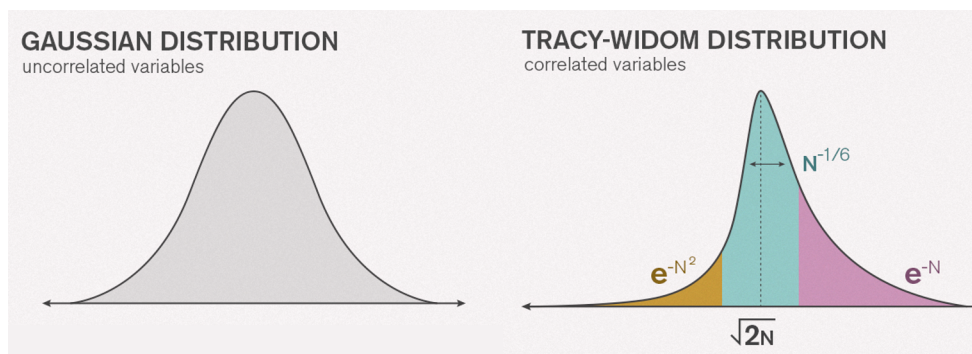


Figure 1.4: Comparison between the shapes of the Gaussian and the Tracy-Widom probability distribution functions (edited from [38]).

Variations of the aforementioned models are used to describe kinetic roughening processes with slightly different features. In particular, as stated in the introduction, we are keen on those in which the noise term  $\eta(x, t)$  presents long-term temporal correlations. In the one-dimensional case, the evolution of the critical exponents in these systems is well known for linear models. However, we have little information about non-linear models, specifically the KPZ equation. This is studied in detail in Chapter 4.

### 1.3 Numerical methods

Our work consists in the study of one-dimensional systems, which have been discretized in order to carry out numerical simulations. This way, we have used a one-dimensional discrete periodic domain  $0 \leq x < L$  with  $\Delta x = 1$ , that is to say, a sequence of  $L$  equidistant positions where the positions  $x = 0$  and  $x = L$  are equivalent. The use of finite systems with periodic boundary conditions is a common choice for simulating very large (or infinite) systems. For increasing values of  $L$ , this discretization scheme models the system as a sequence of positions which approaches the behaviour of large systems or the continuum. Since our time was not infinite either, we needed to find a balance between relatively short computation times and large enough systems that

yield relevant results. In addition, powers of 2 have been used for a more efficient computation of the fast Fourier transform. Therefore we have set the largest size at  $L = 2^{13} = 8192$ , and used lower sizes, starting at  $L = 2^7 = 128$ , to study scaling properties.

The time is discretized with a convenient step  $\Delta t$  in each chapter, with the purpose of achieving an improved numerical precision when fixing the rest of parameters around the unit, as wished. This way, we have used  $\Delta t = 10^{-2}$  in Chapters 2 and 3, while we have needed to set  $\Delta t = 10^{-3}$  when introducing a source of correlated noise in Chapter 4 in order to get stable simulations.

### 1.3.1 Integration scheme for the Burgers equation

Most of the simulations performed over the whole work consist of integrating the complete one-dimensional Burgers equation with conserved noise

$$\partial_t u = \nu \partial_x^2 u + \lambda u \partial_x u + \partial_x \eta, \quad (1.26)$$

where the noise term can be set to zero when integrating the deterministic Burgers equation (Chapter 2). The Euler finite-difference method is the scheme used for its integration. For any position  $j$  of the system,  $0 \leq j < L$ , the updated velocity at position  $j$  is computed according to [33]

$$u_j(t + \Delta t) = u_j(t) + \delta_t u_j \Delta t + \sqrt{2D\Delta t}(\eta_j - \eta_{j-1}), \quad (1.27)$$

where  $D$  is the noise strength and the deterministic derivative  $\delta_t u_j$  is given by

$$\delta_t u_j = \nu (u_{j+1} - 2u_j + u_{j-1}) + \frac{\lambda}{6} (u_{j+1}^2 + u_j u_{j+1} - u_{j-1} u_j - u_{j-1}^2) \quad (1.28)$$

Periodic boundary conditions are considered. This method is particularly convenient for integrating the stochastic Burgers equation, as it provides precise, numerically stable solutions and ensures that the properties of the stationary state are preserved.

Provided that it satisfies the conditions in eq. (1.19), the details of the noise distribution are not relevant for the results, and therefore we used uniform noise with zero mean and unit variance as uncorrelated noise in Chapter 3. We next describe the method used for generating correlated noise.

### 1.3.2 Generation of long-time correlated noise

In Chapter 4 we introduce temporal correlation in the noise term of Burgers equation. Thus, we were interested in generating long time series of noise with long temporal correlation at every position  $x$  of our domain. More specifically, we wished to generate random numbers  $\eta(x, t)$  so that  $\eta(x, t_0)$  is an uncorrelated sequence for fixed  $t_0$ , while  $\eta(x_0, t)$  exhibits long correlations (at least larger than the surface saturation time) for fixed  $x_0$ . Mathematically, this can be expressed by the following correlation relation:

$$\langle \eta(x, t) \eta(x', t') \rangle \propto \delta(x - x') |t - t'|^{2\theta - 1}, \quad (1.29)$$

where the exponent  $\theta \in [0, 1/2)$  quantifies the temporal correlation, which vanishes for  $\theta = 0$  and increases when  $\theta$  does.

With this aim, we have implemented the noise generator successfully used in [1], which builds  $L$  independent sequences with long-range temporal correlation by means of Mandelbrot's fast fractional Gaussian noise generator [24]. The relevance of this method lies on the fact that it does not generate the whole sequence  $Z_j(t)$  at the beginning of the simulation, like other popular methods for generating power-law correlations do, but just uses the previous temporal step. This way, we avoid using a massive amount of computer memory that would restrict the maximum reachable time in simulations. We next explain its basics, and check that the obtained noise does have the properties we wish.

We will focus on one fixed position, and compute the temporal sequence  $Z(t)$  generated as correlated noise. The value of  $Z(t)$  is defined as the weighted sum of certain number  $N$  of Markov-Gauss processes  $X(t, r_n | \text{MG})$  with unit variance and covariance  $r_n = e^{-B^n}$ , where  $B > 1$  can be conveniently chosen:

$$Z(t) = \sum_{n=1}^N W_n X(t, r_n | \text{MG}). \quad (1.30)$$

The weights are given by [24]

$$W_n = \frac{2\theta(1/2 + \theta) (B^{1/2-\theta} - B^{-1/2+\theta}) B^{2(\theta-1/2)n}}{\Gamma(2 - 2\theta)}, \quad (1.31)$$

where  $\Gamma$  is the complete Gamma function. The number of terms  $N$  in eq. (1.30) can be chosen depending on the balance between accuracy and computational cost. One can use a quality factor  $Q$  to estimate the value of  $N$  as function of the wished correlation time  $T$ :

$$N(T) = \frac{\log(QT)}{\log(B)}. \quad (1.32)$$

Lastly, we define the Markov-Gauss processes with the following recurrence rule: for  $t = 0$ , all of them are Gaussian white noises  $\xi_n(t)$ , while for higher times we have

$$X(t, r_n | \text{MG}) = r_n X(t - \Delta t, r_n | \text{MG}) + \sqrt{1 - r_n^2} \xi_n(t), \quad (1.33)$$

where  $\xi_n(t)$  is a white noise [1].

We checked that the actual correlation obtained from the series  $Z(t)$  is the one we expect. We worked with the time Fourier transform of the noise,  $\hat{Z}(\omega)$ , whose correlation function should be approximated in the low frequency limit  $\omega \rightarrow 0$  as [18]

$$\left\langle \left| \hat{Z}(\omega) \right|^2 \right\rangle \propto \omega^{-2\theta}. \quad (1.34)$$

This way, we can easily visualize the behaviour of the correlation at very long times, which would be less feasible when directly working with  $Z(t)$ . As was the case in [1], setting the parameters  $B = 3$  and  $Q = 100$  worked for us (so far: check in the end).

Fig. 1.5 is an example of how the power spectrum density  $S(\omega) := \left\langle \left| \hat{Z}(\omega) \right|^2 \right\rangle$  satisfactory behaves as expected for  $\theta = 0.40$ . We carry out the same process for a representative selection of exponents  $\theta \in (0, 0.50)$ , as Fig. 1.6 shows. We observe that

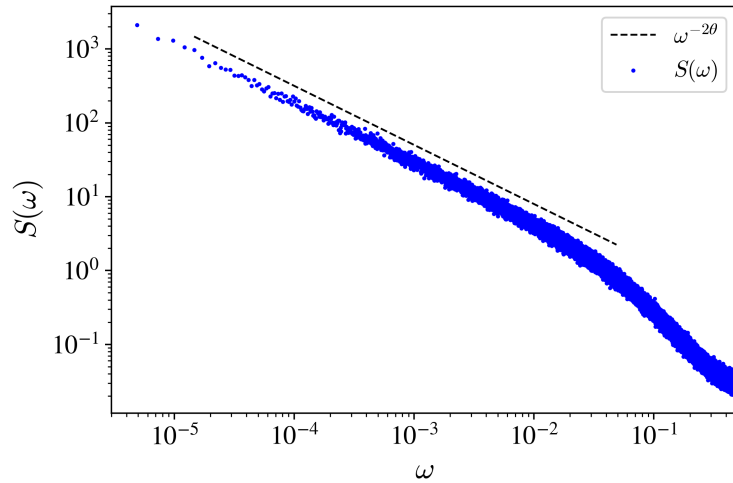


Figure 1.5: Power spectrum density  $S(\omega)$  for a correlation index  $\theta = 0.40$ , and comparison with the expected behaviour  $S(\omega) \sim \omega^{-2\theta}$  as  $\omega \rightarrow 0$ .

the correlations produced by the noise generator essentially match the ones we asked it to, and hence this method can be trusted for introducing temporally long-range correlated noise in stochastic differential equations.

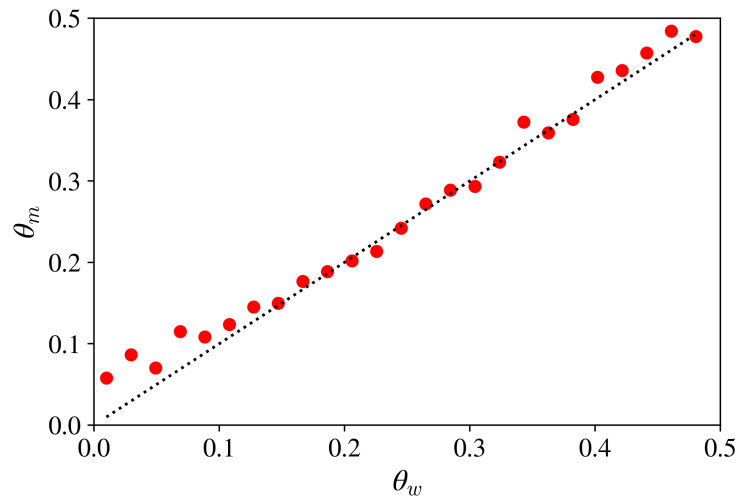


Figure 1.6: Measured values  $\theta_m$  of the correlation exponent for the noise generated using the Mandelbrot scheme, in comparison with the wished values  $\theta_w$ . The dotted line represents the straight line  $\theta_m = \theta_w$ .

## 2 The deterministic Burgers equation

In this chapter we study the one-dimensional, not driven Burgers equation,

$$\partial_t u = \nu \partial_x^2 u + \lambda u \partial_x u, \quad (2.1)$$

where we define  $u = u(x, t)$  on the domain  $0 < x < L$  with periodic boundary conditions  $u(0, t) = u(L, t)$  for all  $t \geq 0$ , as in the rest of the work. This equation is a deterministic second order partial differential equation, whose solutions are uniquely determined for a fixed initial condition  $u(x, 0) = f(x)$ .

The expression above was introduced by H. Bateman [6] in 1915 to better understand the motion in fluids, and later studied by J. M. Burgers [8] as a simpler model than Navier-Stokes describing turbulence. Both equations actually share some characteristics, such as the same type of advective non-linearity, the presence of a diffusion term that allows to define a Reynolds number, and many common invariance and conservation laws. However, the Cole-Hopf transformation provides analytical, explicit solutions for the Burgers equation, as we show next, meaning that it lacks of one of the most unique aspects of turbulence: a highly chaotic behaviour [16].

Therefore, the scope of Burgers equation as a model of turbulent systems is not comparable with that of Navier-Stokes. Despite that, many applications in various fields have been found since its introduction, one of them being our main object of study: its relation with the KPZ equation in statistical physics. We are keen on understanding the deterministic equation first and showing analytical and numerical results, in order to get useful information for our final goal regarding the stochastic equation. We further note that the parameter  $\lambda$  is set to  $-1$  when the equation is used to describe fluids, however we will not fix it and use it as a quantifier of non-linearity, as it is generally the case in KPZ.

### 2.1 An exact solution: the Cole-Hopf transformation

As we commented above, the Burgers equation is non-linear, just as Navier-Stokes, but it admits a change of variables that transforms it into the heat equation, which is linear. Indeed, let us consider a primitive function of the velocity field, i.e. a function  $h(x, t)$  such that  $\partial_x h = u$ , and define  $\phi(x, t)$  according to

$$h(x, t) = \frac{2\nu}{\lambda} \log(\phi(x, t)), \quad (2.2)$$

where the logarithm is defined in an arbitrary base. This is called the Cole-Hopf transformation. Let us see how we can describe the time evolution of  $\phi$ . First we use eq. (2.1) and obtain

$$\partial_t h = \partial_t \left( \int u dx \right) = \int \partial_t u dx = \int \nu \partial_x^2 u dx + \int \lambda u \partial_x u dx = \nu \partial_x^2 h + \frac{\lambda}{2} (\partial_x h)^2. \quad (2.3)$$

Next we consider the relations

$$\partial_t h = \frac{2\nu}{\lambda} \frac{\partial_t \phi}{\phi}, \quad \partial_x h = \frac{2\nu}{\lambda} \frac{\partial_x \phi}{\phi}, \quad \partial_x^2 h = \frac{2\nu}{\lambda} \frac{1}{\phi^2} [\phi \partial_x^2 \phi - (\partial_x \phi)^2].$$

Replacing in (2.3) and multiplying by  $\lambda\phi/2\nu$  yields

$$\partial_t\phi = \nu\partial_x^2\phi, \quad (2.4)$$

which corresponds to the heat equation, a paradigm of linear partial derivative equations, whose solutions have hence been studied in detail. Nonetheless, the non-linearity of the transformation leads to solutions that are not easy to work with.

We can also define periodicity conditions for  $h$ , and subsequently for  $\phi$ , getting  $\phi(0, t) = \phi(L, t)$  for  $t > 0$ . The initial condition is transformed into  $\phi(x, 0) = \Theta(x) := e^{\frac{\lambda}{2\nu}F(x)}$ , where  $F$  is a primitive of  $f$ . With this, the general solution of eq. (2.4) is given by [11]

$$\phi(x, t) = \int_0^L \left( \frac{1}{L} \int_{\mathbb{R}} e^{ik(x-y)} e^{-\nu k^2 t} dk \right) \Phi(y) dy =: \int_0^L H(x-y, t) \Phi(y) dy, \quad (2.5)$$

The function  $H(x, t)$  is called *heat kernel*, and in this case it can be explicitly expressed as [23]

$$H(x, t) = \frac{1}{\sqrt{4\pi\nu t}} e^{-\frac{x^2}{4\nu t}}.$$

Bringing back the original variables into (2.5) yields

$$u(x, t) = -\frac{1}{\lambda} \frac{\int_0^L \frac{x-y}{t} e^{-\frac{(x-y)^2}{4\nu t} + \frac{\lambda}{2\nu} \int_0^y f(z) dz} dy}{\int_0^L e^{-\frac{(x-y)^2}{4\nu t} + \frac{\lambda}{2\nu} \int_0^y f(z) dz} dy}. \quad (2.6)$$

In this way, the Cole-Hopf method allows us to obtain an analytical expression for the solutions of the one-dimensional Burgers equation for any initial condition with good properties. However, it is not straightforward to easily describe or understand how these solutions behave. One of the common strategies to face this problem is to use the method of characteristics. It will be studied in detail for the non-viscous case ( $\nu = 0$ ), since the original method can only be applied to first-order equations, although there exist generalizations for higher orders.

## 2.2 The inviscid equation

The inviscid Burgers equation is obtained by removing the diffusion coefficient  $\nu$  in eq. (2.1):

$$\partial_t u = \lambda u \partial_x u. \quad (2.7)$$

This equation belongs to the class of first order quasilinear hyperbolic equations, that is to say, a hyperbolic equation of first order whose coefficients may depend on the function but not on its derivatives. More specifically, it is a conservative equation, in which the average value  $\bar{u}(t)$  of the field  $u(x, t)$  is conserved over time. Indeed, we show this for a periodic system with size  $L$ :

$$\frac{d\bar{u}(t)}{dt} = \frac{d}{dt} \left( \frac{1}{L} \int_0^L u dx \right) = \frac{1}{L} \int_0^L \partial_t u dx = \frac{\lambda}{2L} \int_0^L \partial_x (u^2) dx = \frac{\lambda}{2L} u^2 \Big|_{x=0}^L = 0,$$

where we have used Leibniz integral rule in the first equality. This leads to the following decomposition of energy, setting  $\bar{u} := \bar{u}(t) = \bar{u}(0)$ :

$$E(t) \propto \frac{1}{L} \int_0^L u^2 dx = \frac{1}{L} \int_0^L (u - \bar{u})^2 dx + \bar{u}^2 = W^2(t) + \bar{u}^2, \quad (2.8)$$

where  $W(t) = \left( \frac{1}{L} \int_0^L (u - \bar{u})^2 dx \right)^{1/2}$  is the roughness of the velocity field, analogous to the surface roughness defined in eq. (1.1), and which can be discretized the same way. This decomposition allows to work with the (squared) roughness of the velocity field as a measure of the effective energy of the system with respect to its equilibrium state.

The inviscid equation is often used as a model of non-linear wave propagation. Despite its simple appearance, it leads to solutions showing special features, namely the formation of discontinuities (*shocks*), which makes it an interesting case of study by itself. We discuss this behaviour later, after carrying out an approach to its analytical solutions, by means of the method of characteristics.

### 2.2.1 Method of characteristics

Although the inviscid Burgers equation (2.7) appears to be simpler than the complete equation (2.1), we observe that carrying out the Cole-Hopf transformation is no longer possible. The key point for the term  $\lambda u \partial_x u$  to be absent in eq. (2.4) is the separation of the relaxation term  $\nu \partial_x^2 u$  into two addends, but this is now non-existent. Actually, the function  $\phi(x, t)$  is not well-defined in this case, and the transformation does not make sense.

Nevertheless, as commented above, the solutions of eq. (2.7) can be described through the method of characteristics. For partial differential equations in two variables  $(x, t)$ , this method consists in finding curves  $(x(s), t(s))$  in such a way that the partial differential equation becomes an ordinary differential equation [32]. They are called the *characteristic curves* (or simply characteristics) of the equation. For the inviscid Burgers equation, obtaining the characteristics is especially easy, and their equations are given by

$$\frac{dx}{ds} = -\lambda u, \quad \frac{dt}{ds} = 1. \quad (2.9)$$

We can hence assume  $t = s$ , and we get

$$\frac{du(x(t), t)}{dt} = \partial_x u \frac{dx}{dt} + \partial_t u = -\lambda u \partial_x u + \partial_t u = 0. \quad (2.10)$$

In other words,  $u(x(t), t)$  is constant on the characteristics, and therefore equals the initial value  $u(x_0, 0) = f(x_0)$ . Reconsidering eq. (2.9), it is now straightforward to solve the first equation and get

$$x(t) = x_0 - \lambda u(x_0, 0)t = x_0 - \lambda f(x_0)t. \quad (2.11)$$

The characteristics are then straight lines with slope  $-1/\lambda f(x_0)$  on the  $(x, t)$  plane, along which the value of  $u$  is constant and equals  $f(x_0)$ . The solution takes the implicit form

$$u(x, t) = u(x_0, 0) = f(x_0) = f(x(t) + \lambda f(x_0)t), \quad (2.12)$$

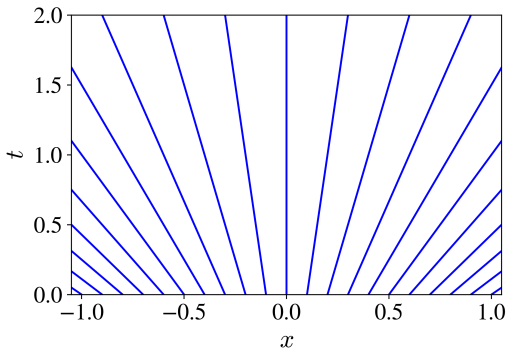


Figure 2.1: Characteristics curves for  $f_I(x) = -x$ .

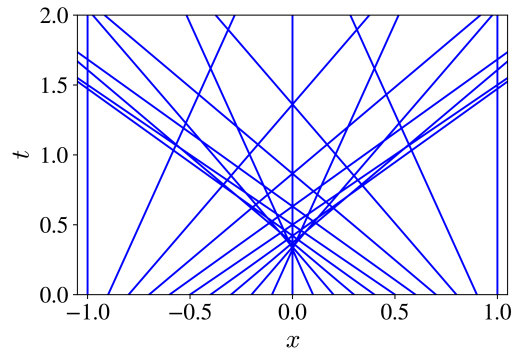


Figure 2.2: Characteristics curves for  $f_{II}(x) = \sin(\pi x)$ .

where  $x$  and  $x_0$  are related according to eq. (2.11). An explicit solution can only be obtained in the simplest cases, e.g. if  $f$  is linear in  $x$ . Nonetheless, the main problem of this solution is not its implicit nature, but solving the intersections between the characteristics that most initial conditions lead to. Let us detail this point.

As an example, we extend the domain  $(0, L)$  to an infinite one,  $-\infty < x < \infty$ , and consider two different initial conditions for eq. (2.7), given by  $f_I(x) = -x$  and  $f_{II}(x) = \sin(\pi x)$ . Figs. 2.1 and 2.2 show the characteristics in both cases. In the case of  $f_I$ , we can observe that the straight lines diverge for  $t > 0$ , coming from a common intersection point at  $t = -1$ . The solution given in eq. (2.12) determines a value  $u(x, t)$  for every point  $(x, t)$  on the upper half-plane, and therefore Burgers equation is solved. However,  $f_{II}$  leads to multiple intersections between the characteristics, in which  $u(x, t)$  is not well-defined. In this case the system's evolution can only be described for small times, prior to reaching the first intersection. Actually, if no regularity is imposed to initial conditions, intersections can be found for arbitrarily small times, provoking a singularity at  $t = 0$ . If the initial condition is not differentiable, there can also exist points  $(x, t)$  such that no characteristic crosses them, and again we cannot define  $u$  on those.

In order to solve this, we need to introduce the concept of *weak solution*, which a priori has less good properties than a classical solution. For instance, a weak solution need not be differentiable or may be only piece-wise continuous [32]. Intersections between characteristics give rise to a discontinuity in  $u(x, t)$  between the values of the two lines, which is called a *shock*. This discontinuity typically moves with time at a velocity related to both values, producing a so-called *shock wave*. This phenomenon is later analysed when solving Burgers equation. The time at which the two first characteristics intersect, and therefore the first discontinuity is observed, is known as *breaking time*.

Selecting the physically correct weak solution requires additional criteria, such as searching for the solution with highest entropy. It can be checked that this is equivalent to computing the exact solutions via eq. (2.6) in the limit  $\nu \rightarrow 0$ . A graphical way to obtain this solution is to use Maxwell's equal area rule, according to which the  $x$  coordinate at which the discontinuity must be located is such that the areas enclosed by the multivalued field and by the shock wave coincide [16, 32]. The method is depicted in Fig. 2.3.

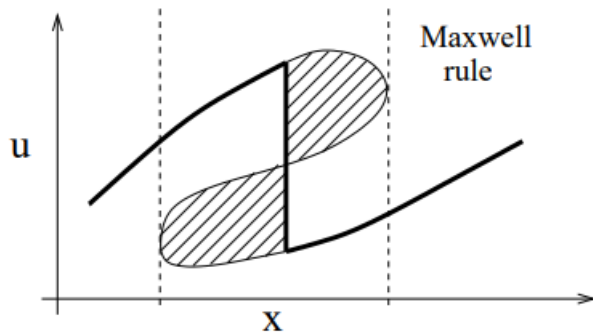


Figure 2.3: Graphical illustration of Maxwell's rule [16].

Back in a periodic domain of length  $L$ , we observe that any non-constant initial condition  $u(x, 0) = f(x)$  yields two characteristics with different slopes, which therefore cross at some point. The example in Fig. 2.2 is selected to show this situation, taking  $L = 2$  and  $-1 \leq x \leq 1$ . We will later collect results of the numerical integration of the inviscid Burgers equation as a particular case of the viscous equation, and identify these features. The numerical solution will give an idea of how the crossings of characteristics are solved and show the formation and evolution of the shocks.

### 2.3 The general form: viscous Burgers equation

We now consider the complete deterministic Burgers equation (2.1), with non-vanishing viscosity. The viscous term is a relaxation term, which quantifies the resistance of the system to being deformed, and therefore implies dissipation of energy, no longer resulting in a conservative equation. Any physical system is actually subject to dissipative forces, so a correct estimate of viscosity will provide a better description of a real fluid than the inviscid equation. The relevance of the viscous term depends on the value of the *diffusion coefficient*  $\nu$  (also called *kinematic viscosity* following its definition in fluid dynamics).

Nevertheless, the interest of the viscous equation is lower from a mathematical point of view, since the extreme phenomena observed in the inviscid equation (shocks, discontinuous solutions) are dampened when introducing the dissipative term. One cannot anymore use the characteristics to solve the equation, and the radical behaviour caused by  $u$  staying constant on the characteristic lines becomes now smoother.

The next section is dedicated to comparing the time evolution of the system for different values of  $\nu$  through numerical simulations. We will show that solving the inviscid equation yields shock solutions generated when the characteristics cross each other, while rounded shapes arise when the diffusion coefficient is present, due to energy losses.

### 2.4 Numerical integration of the deterministic equation

The deterministic Burgers equation is the simplest equation that we numerically integrate in this work. Thus, in addition to its intrinsic relevance as a model describing the evolution of viscous, one-dimensional fluids, it is useful to check that our numerical

method is efficient and correctly simulates the results expected following theory and literature.

We work with the discretization of the periodic domain  $(0, L)$  explained in section 1.3. The formation of shocks in the solutions of the inviscid Burgers equation, studied in section 2.2, gives rise to relatively large discontinuities, which cause the integration method that we use to be highly unstable when the ratio  $\lambda/\nu$  is large. Therefore, the inviscid equation is not integrated, and instead we present simulations corresponding to approximations with low viscosity showing similar features. Alternative methods provide better results for small  $\nu$  but fail when it is large, as no known method is stable for arbitrary values  $\nu$  [17]. Given that our goal is to integrate the stochastic equation with non-vanishing  $\nu$ , we consider that the approximations that we use perfectly fulfil our study of the deterministic equation.

Related to that, we focus on measuring the observables of interest for the stochastic Burgers equation, explained in section 1.2, and studying their relation to the evolution of the velocity field. Additionally, we check whether the solutions of Burgers equation behave, in the limit of low viscosity, as the method of characteristics predict for the inviscid case, and verified the conservation laws linked to that equation. The system's response to increasing the diffusion coefficient  $\nu$  is also studied.

We next present the results of the simulations. Since the solutions of the deterministic Burgers equation with smooth initial conditions have at most only a small number of discontinuities, 3-dimensional profiles and colour maps proved to be a very clear way to present and analyse the behaviour of the solutions, despite some sharp details appearing due to the instabilities at low viscosity. In addition, we shall calculate the time evolution of statistical observables such as roughness and power spectral density. We keep constant the non-linear parameter  $\lambda = 4$  and use different values of the diffusion coefficient  $\nu$  to study the influence of the ratio  $\lambda/\nu$ . A minimum  $\nu = 0.2$  is used to simulate an *almost* inviscid system.

As for the initial conditions, we have chosen to work with three different functions  $f(x) = u(x, 0)$ :

1. A Gaussian shape

$$f_1(x) = \frac{1}{2} e^{-(x-c)^2/\sigma}, \quad (2.13)$$

centered at some point  $c \in (0, L)$  and with dispersion parameter  $\sigma > 0$ , both conveniently chosen for a better visualization of the solutions. This initial condition allows to easily see how a single central perturbation evolves in time.

2. A sinusoidal function of period  $L$

$$f_2(x) = \frac{1}{2} \sin\left(\frac{2\pi x}{L}\right), \quad (2.14)$$

where the amplitude is chosen for improved numerical stability. The almost inviscid solutions obtained for this initial condition are compared with the characteristics of Fig. 2.2.

3. A random sum of Fourier terms

$$f_3(x) = \frac{1}{2} + \sum_{k=1}^{10} a_k \cos\left(\frac{2\pi kx}{L}\right) + b_k \sin\left(\frac{2\pi kx}{L}\right), \quad (2.15)$$

where  $a_k$  and  $b_k$  are uniformly generated in  $[-0.1, 0.1]$

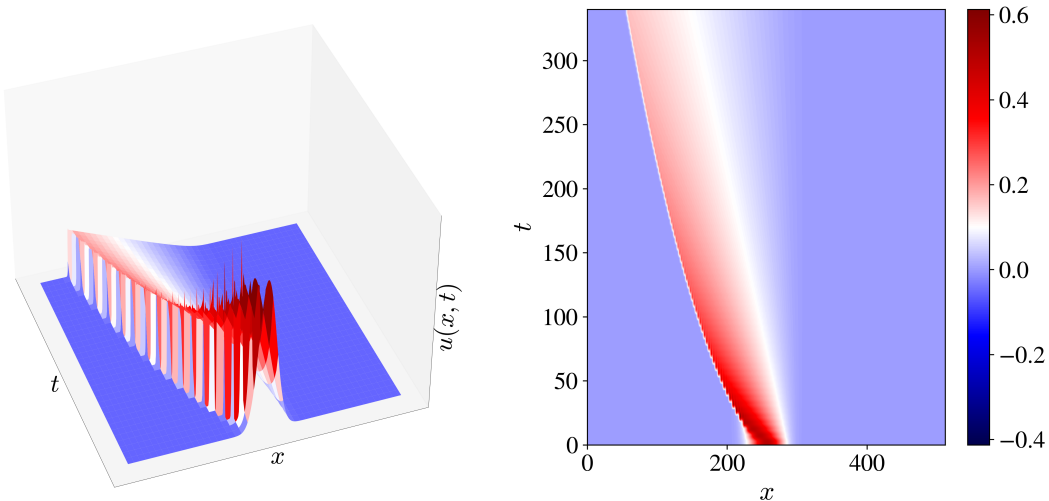


Figure 2.4: Time evolution of the velocity field  $u(x, t)$  for the almost inviscid system ( $\nu = 0.2$ ) of size  $L = 512$ , using the Gaussian initial condition given by eq. (2.13) with parameters  $c = L/2$  and  $\sigma = 512$ . The left panel shows the evolution of the velocity profile along the temporal axis, while the right panel represents its projection on a horizontal plane. The colour and axis scales are the same in both panels.

The time evolution of an almost inviscid system of size  $L = 512$ , with Gaussian initial condition, is depicted in Fig. 2.4. As predicted by the method of characteristics, the initial perturbation moves in the negative direction of the  $x$  axis and the initial shape rapidly becomes sharp, as the shock is formed, showing the typical behaviour of the inviscid Burgers equation. The colour map allows to better observe this transition. The width of the two white bands, for which  $u \simeq 0.1$ , is initially the same and noticeably changes when the first bunch of characteristics cross, as the dark red straight lines are absorbed by lower gradient characteristics. We further notice that the dominant characteristic lines are the ones with lower gradients: the straight lines on the left of the shock cross lower gradient lines and get curved by them, whereas the ones on the right keep their initial constant gradient. We will better visualize this fact when working with sinusoidal initial conditions (Fig. 2.7).

Figs. 2.5 and 2.6 allow to compare the system evolution for different diffusion coefficients. Starting with the same Gaussian initial condition, snapshots at two separate times (Fig. 2.5) show how the shapes get rounder as viscosity is increased, leading to a wider field with the same mean value, which remains constant at  $\bar{u} = 0.039$  no matter the value of  $\nu$ . Fig. 2.6 represents the roughness decay over time. Despite the decay happening faster for greater  $\nu$ , we observe that its shape does not depend on viscosity, vanishing in the  $t \rightarrow \infty$  limit as the system reaches the stationary state. We have carried out a longer simulation for  $L = 256$  and  $\nu = 0.2$ , showing that  $W(t) \sim t^{-1}$  at long times, in accordance with the effective energy decay law  $E(t) \sim W(t)^2 \sim t^{-2}$  deduced analytically for the inviscid case [16]. Lastly, we remark that the roughness corresponding to  $\nu = 0.2$  is approximately constant before suffering a step decay at  $t \simeq 25$ , which seems to match the breaking time when shocks start forming.

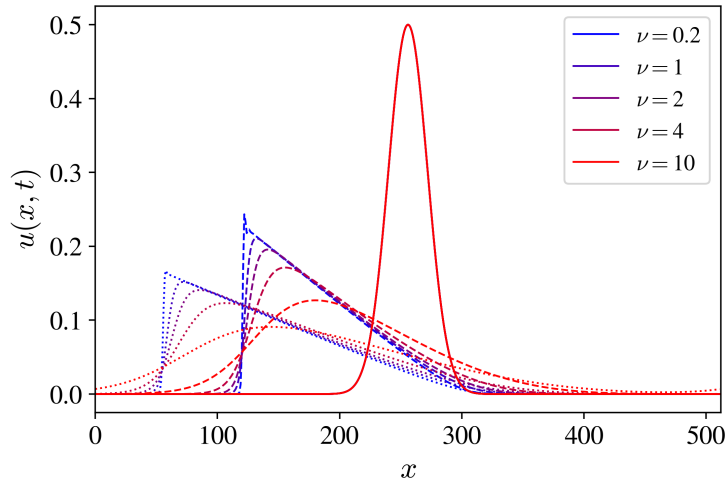


Figure 2.5: Velocity field of the  $L = 512$  system at times  $t = 0$  (solid line),  $t = T/2$  (dashed) and  $t = T = 340$  (dotted) for several values of  $\nu$  with the same Gaussian initial condition. The parameters of eq. (2.13) are set to  $c = L/2$  and  $\sigma = 512$ .

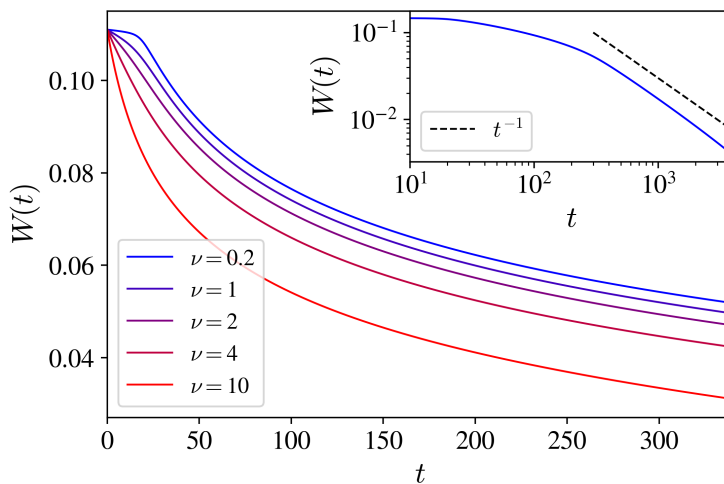


Figure 2.6: Evolution of the system roughness  $W(t)$  for several  $\nu$  in the same conditions as Fig. 2.5. The inset shows the decay of  $W(t)$  at long times for  $L = 256$  and  $\nu = 0.2$ .

This idea is confirmed when looking at Fig. 2.7 (left panel), depicting the time evolution of the almost inviscid system of size  $L = 512$  with the sinusoidal initial condition given by eq. (2.14). First, let us compare the colourmap obtained with the analytical characteristics drawn in Fig. 2.2. While we have now shifted the domain a quarter of a period for a better visualization, the directions of the curves are as expected theoretically, diverging from the  $u = 0$  line at  $x = 128$  towards the one at  $x = 384$ , where the shock is formed. The roughness is essentially constant until reaching the breaking time at  $t \simeq 45$ . This is a consistent result, as the energy is computed by adding up the values of  $u^2$  at each position, which only differ on their location with respect to the initial ones before reaching the breaking time. It is slightly noticeable that the actual diffusion coefficient is not zero, since the white band corresponding to the shock slowly becomes wider. Fig. 2.7 (right panel) corresponds to

a strong viscosity ( $\nu = 10$ ). Now the shock is not formed: the increase of the field value around  $x = 384$  is always smooth and gets flatter at long times. The characteristics are no longer straight lines, but get curved even before crossing, matching the behaviour observed in Fig. 2.6. Regarding the roughness, the decay starts at  $t = 0$ , but an elbow is appreciable at  $t \simeq 45$ .

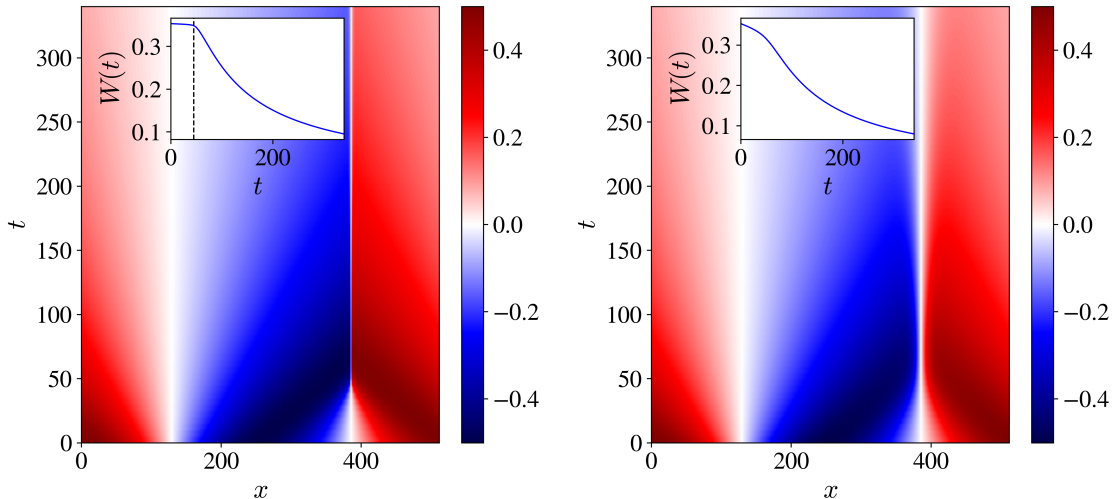


Figure 2.7: Time evolution of the  $L = 512$  system with the sinusoidal initial condition given by eq. (2.14) for  $\nu = 0.2$  (left) and  $\nu = 10$  (right). The insets show the evolution of the roughness  $W(t)$ .

We lastly consider the initial condition  $f_3(x)$  given by eq. (2.15), which represents a more realistic initial state for a system which has been randomly taken away from equilibrium. The results obtained for  $L = 512$  are shown in Fig. 2.8. The left panel, in which the almost inviscid system is simulated, serves as a comparison with respect to the more regular sinusoidal initial condition from Fig. 2.7. Given that  $u(x, 0)$  changes now much faster within the domain, characteristics first cross for very small times (though not zero because of the smoothness of  $f_3$ ). Actually, the complexity of the initial condition rapidly vanishes and only one major shock is found at long times, the system behaving essentially like the one with simpler initial conditions. The analysis of the roughness summarizes this: several elbows can be spotted as the decay starts at small times, before becoming a stable curve for  $t \gtrsim 100$ .

Fig. 2.8 (right panel) depicts the power spectral density (PSD) of the velocity field at several times, together with the 3-dimensional profile describing the evolution of a system of size  $L = 512$  and  $\nu = 2$ , again with initial conditions as in eq. (2.15). This observable gives little information on the deterministic equation, but will be crucial in our study of the stochastic equation in future chapters. One can appreciate that the spectra corresponding to small times show the presence of modes of higher wavenumber corresponding to the multiple initial oscillations. However, these are absorbed into one single shock and the dominant mode is the one with smaller wavenumber  $k = 1/L$  at long times.

All in all, our simulations of the Burgers equation yield satisfying results. The well-known formation of shocks in the low viscosity limit has been observed, presenting features consistent with the theory and matching previously published results [7].

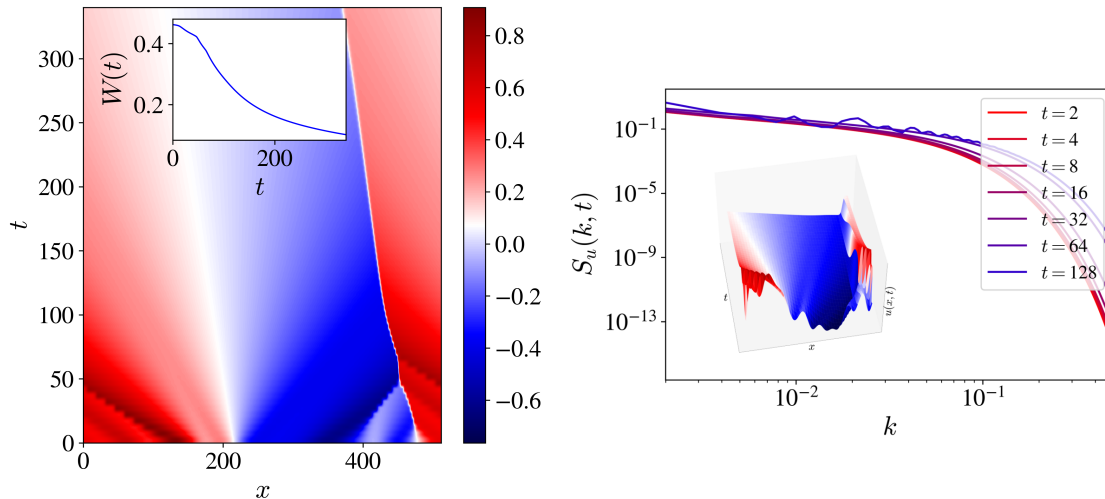


Figure 2.8: On the left, time evolution of the almost inviscid system of size  $L = 512$  with a random initial condition given by eq. (2.15). The inset shows the roughness decay. On the right, PSD at several times of a system with size  $L = 512$  and  $\nu = 2$  for the same kind of initial condition. The evolution of the velocity field is depicted in the inset.

The algorithm used has proved suitable for the deterministic equation, the numerical method being really stable in all cases except  $\nu = 0.2$ , where it presented sharp edges due to the emergence of shocks. In addition, we have successfully measured the time evolution of the roughness and power spectral density, two of our main observables when studying the stochastic equation.

Regarding the deterministic equation on its own, a deeper study would focus on developing accurate integration schemes for the inviscid equation or extending our simulations to more complex initial conditions. For instance, an interesting case is the one of a Brownian initial condition, which can be regarded as the limit of eq. (2.15) with infinite oscillating modes. This is no longer a smooth (nor differentiable) function, provoking the formation of a dense set of shocks at  $t = 0$  when working in a continuous domain [16].

### 3 The stochastic Burgers equation with white noise

In Section 1.2 we discussed several models describing kinetic surface roughening. One of the most important is given by the Kardar-Parisi-Zhang (KPZ) equation, the simplest non-linear out-of-equilibrium model in the continuum showing scale-invariant solutions [20]. We presented the KPZ equation (1.22) in arbitrary spatial dimension  $d$ . Working in  $d = 1$ , the model describes the time evolution of a profile  $h(x, t)$  according to

$$\partial_t h = \partial_x^2 h + \frac{\lambda}{2} (\partial_x h)^2 + \eta(x, t), \quad (3.1)$$

where the coupling constant  $\lambda$  quantifies the strength of non-linearity and  $\eta(x, t)$  is an uncorrelated noise term, whose correlation function is

$$\langle \eta(x, t) \eta(x', t') \rangle = 2\delta(x - x')\delta(t - t'). \quad (3.2)$$

Given its notorious relevance as a central model, not only in surface growth but in many other non-equilibrium phenomena, the KPZ equation has been widely studied in recent times, both analytically and numerically. In fact, the one-dimensional case in which we are interested here has been solved exactly. We review some of the most relevant analytical results in Section 3.2, briefly explaining the methods that have led to them. Existing numerical studies on the equation are in accordance with these analytical results [31]. We shall later compare them with the results of our own simulations in Section 3.3.

In this work we carry out a numerical analysis of the system using a different approach, as we will not integrate the KPZ equation itself. Setting  $u(x, t) := \partial_x h(x, t)$  and taking the spatial derivative in eq. (3.1), we obtain the *stochastic Burgers equation* in one dimension with conserved, uncorrelated noise

$$\partial_t u = \partial_x^2 u + \lambda u \partial_x u + \partial_x \eta. \quad (3.3)$$

The word *conserved* means that the noise term in the Burgers equation is the spatial derivative of an uncorrelated noise, so that  $\int \partial_x \eta dx = 0$  and the mass contribution of the noise term is exactly zero. When we mention the stochastic Burgers equation in this work we will refer to the Burgers equation with conserved noise (3.3). Given that we focus on the KPZ problem, we will not address the equation with non-conserved noise, which exhibits completely different characteristics [31].

The function  $u(x, t)$  represents the slope of the interface  $h(x, t)$  of the KPZ equation at each position of the domain. Alternatively, it can again be interpreted as the velocity field of a one-dimensional fluid with periodic boundary conditions, with the introduction of a conserved white noise modelling the presence of a driving force which randomly stirs the fluid according to  $\partial_x \eta$ .

Our goal in this chapter is to compute the time evolution of the field  $u(x, t)$  and then integrate over  $x$  in order to recover the profile  $h(x, t)$ . By doing so, we will collect the corresponding sets of observables for both fields and measure the scaling exponents relative to each equation. The obtained results can be compared with previous published results on the Burgers equation itself and the direct integration of the KPZ equation.

### 3.1 The multiple regimes of a KPZ system

Just as we did when introducing kinetic roughening processes in Section 1.2, we consider a flat initial condition for the height field. In one dimension, this means  $h(x, 0) \equiv 0$  for  $0 \leq x < L$ , or equivalently  $u(x, 0) \equiv 0$ . Taking a look into eq. (3.1), a flat interface at  $t = 0$  means that the only non-negligible term in the first time steps is the noise term, and thus the KPZ equation behaves as a random deposition process

$$\partial_t h \simeq \eta(x, t) \quad (3.4)$$

for very small  $t$ . The random deposition model might not accurately describe any physical system in the long term, since the absence of diffusion means no information transfer between adjoining positions and no correlations, which is not too realistic. However, as we have suggested and our simulations will confirm, systems subject to the KPZ or EW equations, or in general any of the models presented in Section 1.2, behave according to the random deposition model at small time scales, implying that random deposition is actually a very relevant model in surface growth, at least for short-time scales.

Likewise, given that the shape of the interface at short times is essentially controlled by the noise term, the height field is highly non-smooth and the first and second derivatives  $\partial_x h$ ,  $\partial_x^2 h$  take similar values in average. This makes the linear term dominate in the following time steps, as it is not squared, and the system behaves according to the EW model

$$\partial_t h \simeq \partial_x^2 h + \eta(x, t). \quad (3.5)$$

We will better understand this behaviour using scaling arguments in the next section. The opposite effect is observed at long times, with the non-linear term being dominant. Thus, the KPZ regime is said to be the *asymptotic* regime of this kind of systems.

While a random deposition stage is generally observed when simulating the KPZ equation, the coupling constant  $\lambda$  determines how distinct the linear and the non-linear regimes are. Subsequently, we will compare the evolution of the system for two different values of  $\lambda$ .

### 3.2 Existing analytical results

We next summarize the most important methods leading to the exact critical exponents in the three models considered above. The linearity of eqs. (3.4) and (3.5) allows a simple and straightforward derivation of the critical exponents. In contrast, for the full KPZ equation we simply give a hint of the main ideas, since a complete analytical study requires more complex approaches which are beyond the scope of this work.

#### 3.2.1 Random deposition

eq. (3.4) can directly be integrated, obtaining

$$h(x, t) = \int_0^t \eta(x, t') dt'. \quad (3.6)$$

Given that  $\langle \eta(x, t) \rangle = 0$ , the average of  $h(x, t)$  vanishes as well, while the noise correlation  $\langle \eta(x, t) \eta(x', t') \rangle = 2D \delta(x - x') \delta(t - t')$  implies

$$\begin{aligned}
\langle h^2(x, t) \rangle &= \frac{1}{L} \int_0^L \left( \int_0^t \eta(x, t') dt' \int_0^t \eta(x, t'') dt'' \right) dx \\
&= \int_0^t \int_0^t 2D\delta(t' - t'') dt' dt'' = 2Dt.
\end{aligned} \tag{3.7}$$

With that, we deduce that  $W^2(t) = \langle h^2 \rangle - \langle h \rangle^2 \propto t$ , meaning  $\beta = 1/2$ . The surface roughness does not reach a saturation value.

### 3.2.2 Edwards-Wilkinson equation

There are two analytical procedures to obtain the critical exponents in the EW equation: direct integration in the Fourier space or the use of scaling arguments [4]. Here we show the second one, since the scaling approach is a useful and elegant tool when it is not possible to integrate the equation analytically.

The main point is that we are looking for scale invariant solutions. The following rescaling of variables in terms of the critical exponents should provide an interface statistically equivalent to the original one, therefore satisfying the same eq. (3.5):

$$\bar{x} = bx, \quad \bar{t} = b^z t, \quad \bar{h} = b^\alpha t, \tag{3.8}$$

where  $b > 0$  is arbitrary. We find the following relations between derivatives:

$$\partial_{\bar{x}}^2 \bar{h} = b^{\alpha-2} \partial_x^2 h, \quad \partial_{\bar{t}} \bar{h} = b^{\alpha-z} \partial_t h. \tag{3.9}$$

Furthermore, given that  $\delta(ax) = \frac{1}{a} \delta(x)$ , the noise term must become  $\bar{\eta} = b^{-1/2-z/2} \eta$  in order to recover the correlation relation. Putting all together, the following equation

$$b^{\alpha-z} \partial_t h = b^{\alpha-2} \partial_x^2 h + b^{-1/2-z/2} \eta \tag{3.10}$$

must be equivalent to eq. (3.5), which yields the relations

$$z - 2 = 0, \quad -\frac{1}{2} + \frac{z}{2} - \alpha = 0, \tag{3.11}$$

and thus we get  $z = 2$ ,  $\alpha = 1/2$  and  $\beta = \alpha/z = 1/4$ .

### 3.2.3 KPZ equation

When we attempt to repeat the same rescaling trick in the KPZ equation, we get

$$\partial_t h = b^{z-2} \partial_x^2 h + \frac{\lambda}{2} b^{\alpha+z-2} (\partial_x h)^2 + b^{-1/2+z/2+\alpha} \eta. \tag{3.12}$$

If  $\alpha > 0$ , as holds for the three equations considered, we can now see that the linear term is dominant at short times, whereas non-linearity controls the behaviour at long times. However, determining the exponents using the same strategy as before is no longer possible, since it would lead to a system of three independent equations with only two unknowns. The key point here is that the coefficients do not rescale independently, as we already saw in Section 1.2.3 when we discussed dimensionless variables

and the rescaled coupling constant  $\bar{\lambda} = \lambda(D/\nu^3)^{1/2}$ . Therefore, simple power-counting fails for the full KPZ equation.

Thus, other more sophisticated techniques must be used to determine the critical exponents in the case of KPZ, as well as in other non-linear growth models. Systems in the KPZ universality class satisfy an important symmetry, the Galilean invariance, which leads to a useful scaling relation between the critical exponents  $\alpha$  and  $z$ .

The property of Galilean invariance is exhibited by the systems whose behaviour remains the same in any inertial frame of reference [13]. We show this in the case of the KPZ equation by performing the following infinitesimal transformation in terms of a small  $\epsilon > 0$ :

$$\begin{aligned}x' &= x - \lambda\epsilon t, \\t' &= t, \\h' &= h + \epsilon x.\end{aligned}\tag{3.13}$$

The transformed equation is the same as eq. (3.1) except for the terms  $\mathcal{O}(\epsilon^2)$ . However, since we are considering an infinitesimal transformation, these terms can be neglected and we recover the KPZ equation for the new variables, meaning the system is Galilean invariant. This is actually an exact symmetry, given that checking infinitesimal transformations is sufficient according to the Ward identity [9].

Considering the Burgers equation for the variable  $v' = -u' = -\partial_x h'$  is equivalent to setting  $\lambda = -1$  in eq. (3.3), which is generally done when the equation is used to describe fluids as we pointed out in Chapter 2. This way, we may write the Galilean transformed Burgers equation as (dropping tildes)

$$\partial_t v + v\partial_x v = \partial_x^2 v + \partial_x \eta,\tag{3.14}$$

where the left-hand side is actually the total derivative

$$\frac{dv}{dt} = \partial_t v + \frac{dx}{dt} \cdot \partial_x v = \partial_t v + v\partial_x v\tag{3.15}$$

which must hold upon rescaling. In other words, Galilean invariance allows us to transform the KPZ equation for any  $\lambda$  in an equation like (3.14), forcing the relation between the non-linear term  $\frac{\lambda}{2}(\partial_x h)^2$  and the time derivative  $\partial_t h$  to be the same after rescaling. Back into eq. (3.12), this is achieved if and only if

$$\alpha + z = 2\tag{3.16}$$

holds. This relation is called the *Galilean invariance* of the KPZ equation and is not shared by other models describing kinetic roughening, which makes it a very relevant feature of KPZ. Despite the fact that our derivation is performed for  $d = 1$ , the relation is valid for any dimension, allowing to focus on computing just one of the critical exponents. A similar calculation can be carried out for the Burgers equation with conserved noise yields  $\alpha + z = 1$ .

Having the critical exponents  $\alpha$  and  $z$  constrained to satisfy eq. (3.16) means that we only need to determine one of them independently. In one dimension, the roughness exponent  $\alpha$  can be computed by means of the fluctuation-dissipation theorem [4, 9]. We start by considering a general Langevin equation

$$\partial_t h = G(h) + \eta(t)\tag{3.17}$$

for every position  $0 \leq x < L$ , and associate it with a Fokker-Planck equation which describes the time evolution of the probability that the interface reaches a certain height at each position. Details can be found in [4]. One can then find a probability distribution which is a solution of the Fokker-Planck equation and deduce that the shape of the interface is exactly a Brownian motion. As a consequence,  $\alpha = 1/2$ , and following eq. (3.16), we get  $z = 3/2$  and  $\beta = 1/3$ . This way, we have obtained the exact critical exponents of the KPZ equation for  $d = 1$ . Similarly, for the one-dimensional Burgers equation one gets  $\alpha = -1/2$  and  $z = 3/2$ .

It is important to remark that the use of the fluctuation-dissipation theorem is not possible in higher dimensions, and thus the determination of the critical exponents requires more laborious methods for  $d > 1$ . One of the most successful tools in that sense is the dynamic renormalization group (DRG) approach, which provides a systematic approximation of the large-scale behaviour of the system. It is based on an iterative solution in Fourier space in terms of Green functions with a coarse-graining stage to eliminate small scales and a later rescaling [31]. The critical exponents are then obtained from the so-called *flow equations* in the form of a perturbative expansion series.

In recent years, multiple authors have presented alternative analytical methods for obtaining the critical exponents of the KPZ equation or other equations of the same universality class, which present the same set of scaling exponents, such as directed polymers in random media or asymmetric simple exclusion processes. Some of these problems, as well as the KPZ equation under certain initial conditions, admit a complete, exact analytical solution [22]. One prominent example is the study of the fluctuations of the particle flux for discrete time (dTASEP, discrete totally asymmetric simple exclusion process) carried out by K. Johansson, which reveals the close relation between the KPZ universality class and the theory of random matrices [19]. A review on the most basic analytical results about the KPZ equation can be found in [29].

### 3.3 Numerical integration of the stochastic equation with uncorrelated noise

As we have seen, a lot of effort has been put into the KPZ equation with uncorrelated noise since it was first proposed in 1986. Specifically, the one-dimensional case is well understood analytically: not only the exact values of the critical exponents are known, but the solution  $h(x, t)$  has also been determined.

The aim of this section is to compare our numerical simulations with the existing analytical results. By doing so, we shall check that our numerical method, which proved to be successful for integrating the deterministic Burgers equation, is equally valid for the stochastic Burgers equation. Moreover, we use different techniques for measuring the critical exponents, that will become important in Chapter 4 when computing them for different correlation intensities.

Just as we did with the deterministic equation, we consider again the discretization of the system described in Section 1.3. We will compare systems of sizes between  $L = 128$  and  $L = 8192$ . In this case we will set the initial condition  $u(x, 0) \equiv 0$ , i.e. we start from a flat interface  $h(x, 0)$ , following the definition of the scaling exponents in Section 1.2. Regarding the coupling constant  $\lambda$ , we shall analyse simulations for

$\lambda = 4$  and  $\lambda = 8$ . Both values are small enough to ensure the numerical stability of the simulations, while they provide an interesting comparison of the transitions through different growth regimes explained in Section 3.1, as we shall see. Under these conditions, eq. (3.3) is integrated using the numerical scheme explained in Section 1.3, and the observables defined in Section 1.2 were computed at a conveniently chosen set of times for both the field  $u(x, t)$  and its primitive field  $h(x, t) = \int u(x, t)dx$ . We next present the obtained results.

The time evolution of the surface roughness is depicted in Fig. 3.1 ( $\lambda = 4$ ) and Fig. 3.2 ( $\lambda = 8$ ). Several regions with different slopes  $\beta$  are present, corresponding to the time scales in which the different growth regimes dominate. The system spends the first few time steps in the random deposition regime, with a slope  $\beta = 0.44$  in both cases, before switching to a region of slower growth. The presence of three regimes can be clearly seen in Fig. 3.1 for the system with  $\lambda = 4$ . The roughness grows at a rate  $\beta = 0.26$  until  $t \simeq 10^2$ , while a slope  $\beta = 0.30$  is measured for larger times. As we predicted, the growth exponents suggest that the system goes through the EW regime first and then into the asymptotic KPZ regime. We notice that the values of the exponents are not exact, since the transition between regimes is smooth and thus the observed behaviour does not correspond purely to any of them. This way, the exponent related to random deposition is smaller than the theoretical one, whereas the measured EW and KPZ exponents are closer to each other in comparison with the expected values  $1/4$  and  $1/3$ .

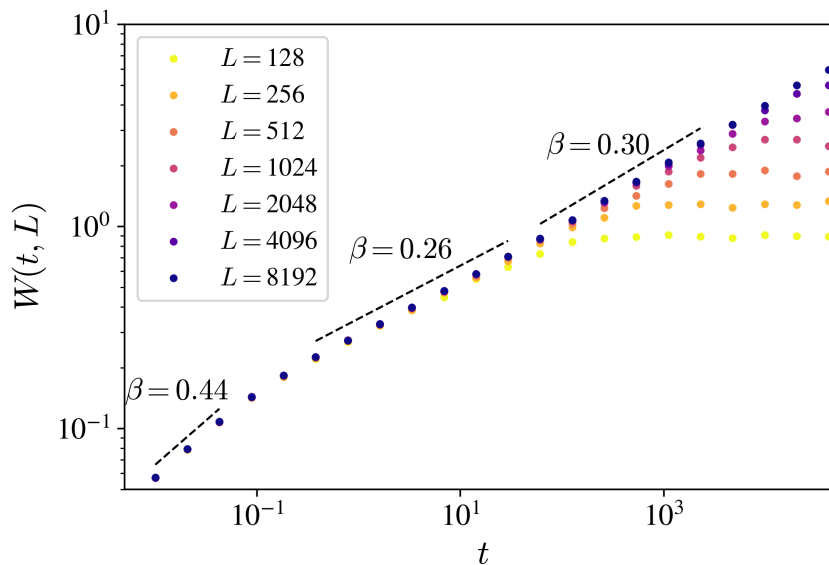


Figure 3.1: Time evolution of the surface roughness  $W(t, L)$  for systems of different lateral sizes for  $\lambda = 4$ . The dashed lines show the slopes of the linear fits in the most representative regions. A logarithmic scale is used in both axes.

Similarly, the system with  $\lambda = 8$  represented in Fig. 3.2 does not properly enter the EW regime, but rather a transition zone leading to an earlier and more characteristic KPZ behaviour as the non-linear coefficient dominates. The roughness describes a concave curve of increasing slope which stabilizes between  $t = 10$  and  $t = 10^2$ . The slope between this point and the saturation time of the largest system is  $\beta = 0.32$ .

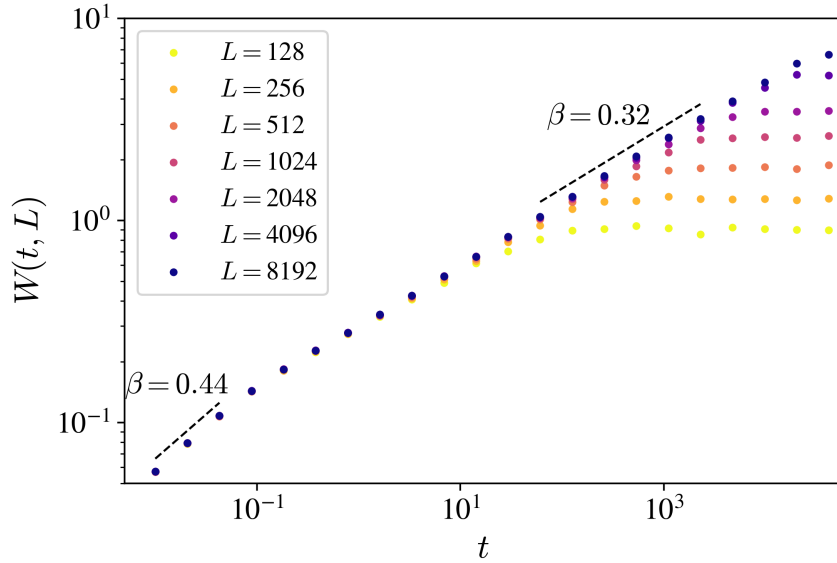


Figure 3.2: Time evolution of the surface roughness  $W(t, L)$  for systems of different lateral sizes for  $\lambda = 8$ . The dashed lines show the slopes of the linear fits in the most representative regions. A logarithmic scale is used in both axes.

This value is closer to the exact  $\beta = 1/3$ , that would be achieved at long time scales for larger systems than the ones we simulated, or alternatively using a larger  $\lambda$ . High computational cost and numerical instabilities have not allowed us to do so.

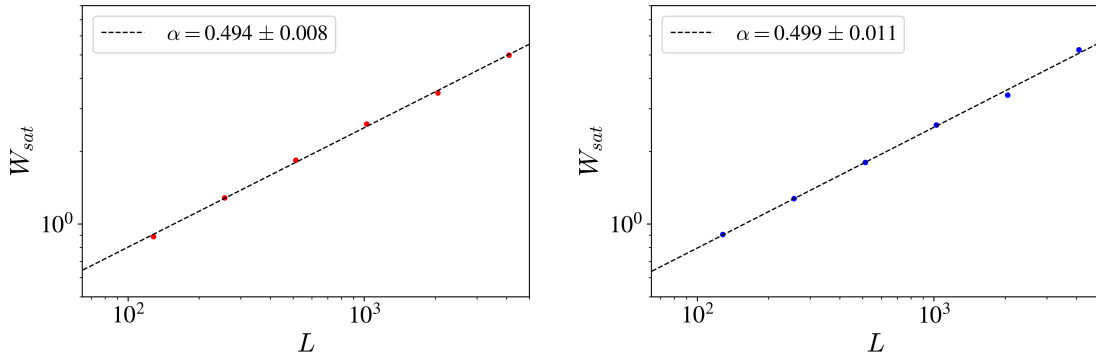


Figure 3.3: Saturation values  $W_{\text{sat}}$  of the surface roughness for lateral sizes between  $L = 128$  and  $L = 4096$  using the data of Fig. 3.1 ( $\lambda = 4$ , left panel) and Fig. 3.2 ( $\lambda = 8$ , right panel). The corresponding linear fits yield roughness exponents  $\alpha = 0.494 \pm 0.008$  and  $\alpha = 0.499 \pm 0.011$ , respectively.

Additionally, Figs. 3.1 and 3.2 allow to compute the roughness exponent  $\alpha$  for both coefficients. With this aim, we plot (Fig. 3.3) the saturation roughness for all sizes except for the largest one (which does not clearly achieve saturation) and performed a linear fit in each case. Since the theoretical prediction for the roughness exponent is the same in both EW and KPZ models, it is not relevant whether a given size saturates in one or another regime and we can consider all sizes at once. The measured slopes are  $\alpha = 0.494 \pm 0.008$  ( $\lambda = 4$ ) and  $\alpha = 0.499 \pm 0.011$  ( $\lambda = 8$ ). Both results are

consistent with the theoretical value  $\alpha = 1/2$  presented in Section 3.2. Note that now we could use either Galilean invariance or the measured  $\alpha$  and  $\beta$  to compute the dynamic exponent  $z$  of the KPZ model. However, the system does not completely reach the asymptotic KPZ regime and we cannot affirm that the Galilean symmetry holds under these conditions, thus a more realistic estimation is to compute the quotients  $\alpha/\beta$  in each case, yielding  $z \simeq 1.67$  for  $\lambda = 4$  and  $z \simeq 1.56$  for  $\lambda = 8$ .

Due to the fact that  $\alpha$  is the same in the EW and KPZ regimes and that saturation is achieved early for most sizes, we are able to obtain a direct and accurate measure of  $\alpha$ . In contrast, when the first clause is not satisfied, as it is the case for  $\beta$  and  $z$ , the measured values are far less accurate. Similarly, determining  $\alpha$  will prove harder when we consider temporally correlated noise in Chapter 4.

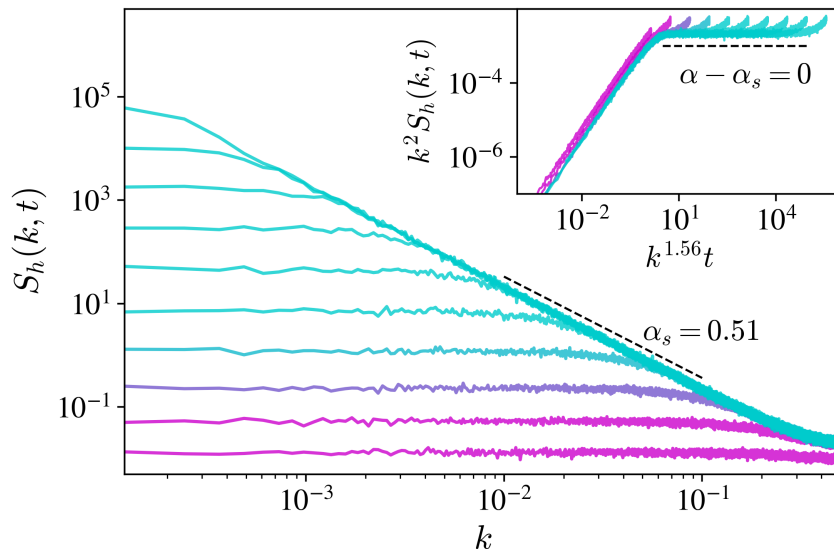


Figure 3.4: Power spectral density  $S_h(k, t)$  of the height field for  $\lambda = 8$  and  $L = 8192$ . Starting at  $t_0 = 0.04$  (purple), each curve represents the PSD for a time 4 times greater than the one below. The inset shows the collapsed data in the KPZ regime according to eq. (1.14), using the exponents measured from the roughness evolution that lead to  $z = 1.56$  and  $2\alpha + 1 = 2$ .

As we argued in Chapter 1, another main observable in the study of kinetic roughening processes is the structure factor or power spectral density. Given that our main goal is the study of the critical exponents of the KPZ equation, we shall first focus on the PSD of the  $\lambda = 8$  system, which behaves closer to the asymptotic KPZ regime according to the roughness evolution. Fig. 3.4 depicts the PSD  $S_h(k, t)$  of the  $L = 8192$  system at increasing times, while the inset shows the collapsed data using the exponents  $\alpha$  and  $z$  measured before. We notice that all curves in blue ( $t \gtrsim 10$ ) merge into a single curve, matching the general behaviour in kinetic roughening described by Fig. 1.3. This suggests that the system enters the KPZ regime slightly earlier than considered before. Following eq. (1.16), the spectral roughness exponent  $\alpha_s$  can be measured directly from the slope  $-(2\alpha_s + 1)$  of the function  $S_h(k, t)$  at large  $t$ . Again, given that the roughness exponent is the same in both growth regimes, the same slope should be obtained in every curve. Therefore, we choose to measure over the upper curve and in a region with a stable slope and enough data. The linear fit performed in that region

yields  $\alpha_s = (0.51 \pm 0.04)$ , the uncertainty being due to the noise in the PSD for the number of realizations done. This value is consistent with the exponent obtained from the roughness evolution, as the inset confirms, since the horizontal shape in the upper part ensures that the relation  $\alpha = \alpha_s$  holds. We conclude that the scaling corresponds to the Family-Vicsek class.

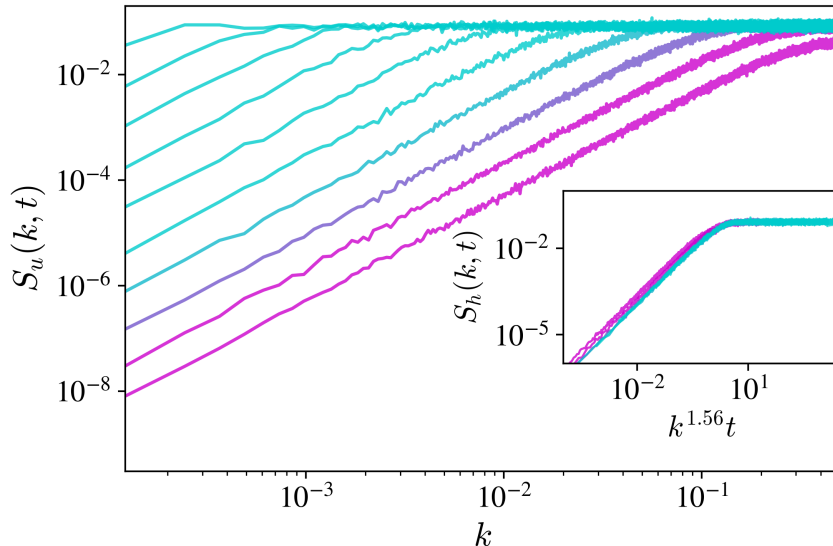


Figure 3.5: Power spectral density  $S_u(k, t)$  of the velocity field for  $\lambda = 8$  and  $L = 8192$ . Starting at  $t_0 = 0.04$  (purple), each curve represents the PSD for a time 4 times greater than the one below. The inset shows the collapsed data in the KPZ regime according to eq. (1.14), using  $\alpha = -1/2$  and again  $z = 1.56$ .

The results obtained from the analysis of the PSD of the velocity field,  $S_u(k, t)$ , do not differ much as compared with those for KPZ. We plot again the case  $\lambda = 8$  in Fig. 3.5. The shape observed matches the one expected when considering eq. (1.14) with  $\alpha = -1/2$ , and this is confirmed by the measured value  $\alpha_s = -0.50 \pm 0.02$ . The collapsed data exhibit the same behaviour as the ones depicted in Fig. 3.4.

Alternatively, the PSD in the case  $\lambda = 4$  allows to distinguish the two growth regimes more clearly by collapsing the data with different scaling exponents. This is done in Fig. 3.6: the pink curves merge into a single curve for  $z = 1.92$ , while the blue curves do in turn for  $z = 1.67$ . The spectral roughness exponent is measured the same way as before, yielding  $\alpha_s = (0.52 \pm 0.04)$ , which is also in this case compatible with the global exponent  $\alpha$ .

While the information given by the PSD of the height field and the velocity field are comparable, the study of the roughness of the field  $u(x, t)$  is not that interesting. Since  $\alpha < 0$  (and thus also  $\beta$ ), these exponents lose their physical meaning and cannot be obtained from the roughness evolution, which shows in fact to be independent (plots not shown) of the size of the system in our simulations.

In the final part of this section, we shall check the properties of the height distribution of the systems that we have simulated. As we saw in Chapter 1, we expect the height distribution to present a different shape in the random deposition and EW regimes than in the proper KPZ regime. Indeed, the theory predicts a Gaussian dis-

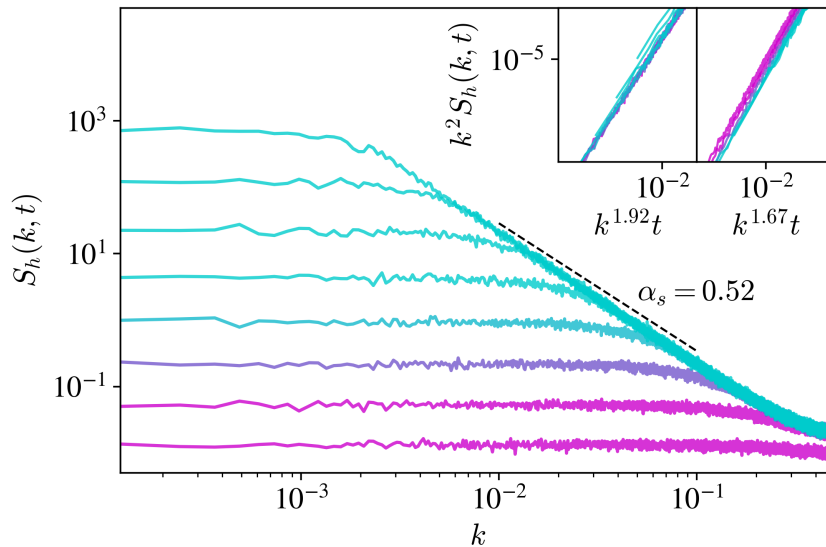


Figure 3.6: Power spectral density  $S_h(k, t)$  of the height field for  $\lambda = 4$  and  $L = 8192$ . Starting at  $t_0 = 0.04$  (purple), each curve represents the PSD for a time 4 times greater than the one below. The insets show the collapsed data in the EW (left) and KPZ (right) regimes, using the exponents measured from the roughness evolution, which lead to  $z = 1.92$  and  $z = 1.67$ , respectively, while  $2\alpha + 1 = 2$  in both cases.

tribution in the first cases and a Tracy-Widom distribution later, which turns back to Gaussian once the system reaches saturation.

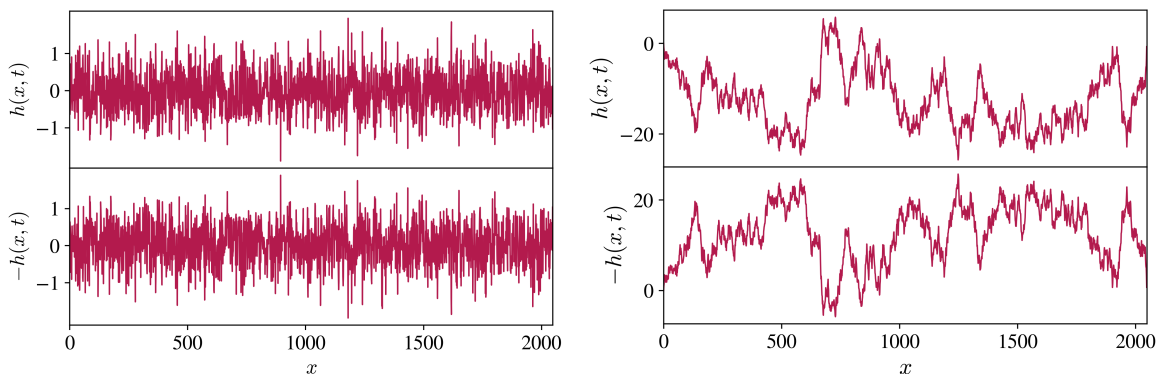


Figure 3.7: Snapshots of the height field of the  $L = 2048$ ,  $\lambda = 8$  system at times  $t = 10^{-1}$  (left panel) and  $t = 10^2$  (right panel), together with their up-down mirror reflections, allowing to study the up-down symmetry of the system at different times.

Taking Fig. 3.4 as a reference for the time scales, we plot in Fig. 3.7 the interface morphology  $h(x, t)$  for  $\lambda = 8$  of the highly non-linear  $L = 2048$  system at times  $t = 10^{-1}$  (random deposition-EW regime, left panel) and  $t = 10^2$  (KPZ regime, right panel). For better detecting how symmetric the distributions are, we also plot their up-down mirror reflections  $-h(x, t)$ . We notice that the snapshot at  $t = 10^{-1}$  shows a seemingly symmetric distribution, essentially indistinguishable from its mirror reflection. In contrast, one can appreciate at first sight that the height field and its reflection at  $t = 10^2$  are different morphologies.

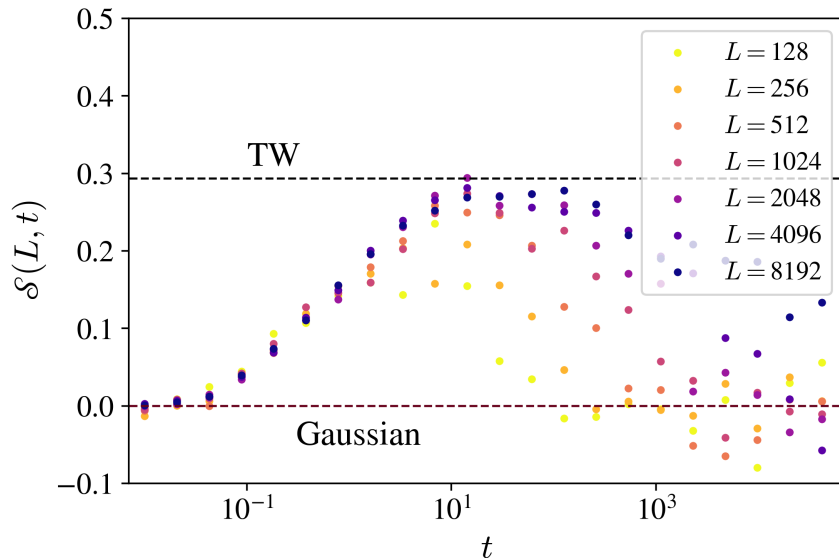


Figure 3.8: Time evolution of the skewness  $\mathcal{S}$  of the height field for  $\lambda = 8$  and several lateral sizes  $L$ . The dashed lines show the theoretical values of the skewness of the Gaussian (red) and TW (black) distributions. The scale in the horizontal axis is logarithmic.

In order to get quantitative evidence, Fig. 3.8 depicts the time evolution of the skewness of the height field  $\mathcal{S}(L, t)$ , defined in eq. (1.3), for several sizes and  $\lambda = 8$ . Now, we notice that the skewness is essentially zero at early times and then grows steadily until stabilizing around the characteristic value of the TW distribution for every size  $L$ , showing a universal behaviour in accordance with the predictions. The values decrease again as the systems with different sizes reach the saturation regime, where the height distribution becomes Gaussian again. Supporting the results in Fig. 3.4, we appreciate that the smaller systems barely visit the KPZ regime, whereas the largest ones do spend quite some time in it. In turn, Fig. 3.9 allows to confirm that the distribution in the intermediate times is in fact a TW distribution. We plot the empirical probability distribution function of the  $L = 2048$ ,  $\lambda = 8$  system at time  $t = 10^2$  averaged over 500 realizations. We observe that the shape of the PDF matches the theoretical TW distribution function, namely exhibiting a remarkable asymmetry, contrary to the Gaussian distribution.

To summarize, we have successfully integrated the stochastic Burgers equation with the numerical scheme described in Section 1.3, using uncorrelated uniform noise with zero mean and unit variance. Under these conditions, the method proves to be stable for a time step  $\Delta t = 0.01$ , for both values  $\lambda = 4$  and  $\lambda = 8$  of the coupling parameter. We expected to simulate the evolution of KPZ systems by integrating the field  $u(x, t)$  resulting from the Burgers equation and thus obtaining  $h(x, t)$ . This has been achieved and the results match the theoretical predictions and previous numerical results for the KPZ equation: multiple regimes (random deposition, EW and finally KPZ) are visited by the system before reaching saturation, while the evolution of the surface roughness follows eq. (1.11) with the expected exponents, the discrepancies being explained by the mixing between regimes. In addition, the PSDs of both fields  $h$  and  $u$  and the exponents extracted from them are in accordance with eq. (1.14), showing that the

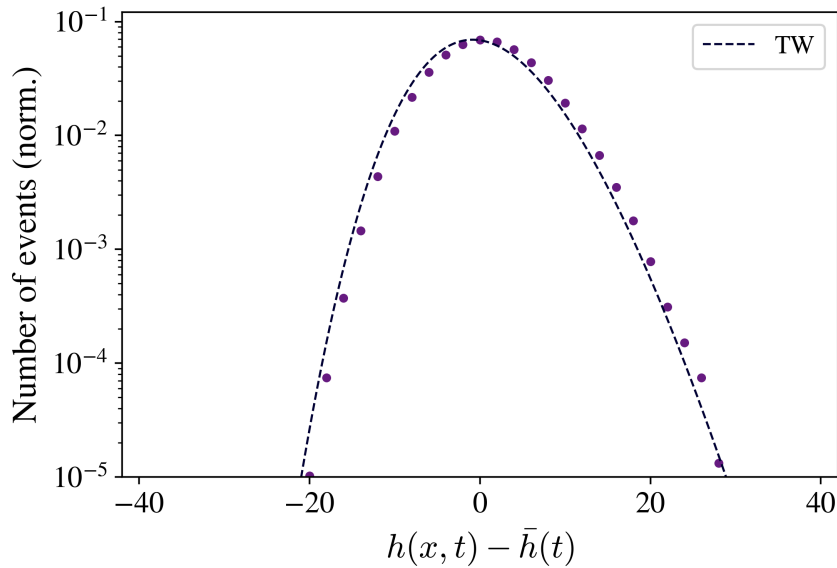


Figure 3.9: Empirical probability distribution function of the fluctuations of the  $L = 2048$ ,  $\lambda = 8$  system at  $t = 10^2$  averaged over 500 noise realizations. The dashed line represents the theoretical probability distribution.

system obeys the Family-Vicsek description with the KPZ exponents. Lastly, we have checked that the distribution of the height field presents up-down symmetry first, as expected for the random deposition and EW regimes, but becomes an asymmetric TW distribution in the intermediate times, following the KPZ behaviour, before turning back to Gaussian in the saturation regime.

The next step is to use a similar integration method to extend these results to the stochastic Burgers equation with long-range temporally correlated noise. Chapter 4 is dedicated to this, with the main goal of studying how the critical exponents evolve as temporal correlations become stronger.

## 4 The stochastic Burgers equation with correlated noise

In the previous chapter, we have integrated the stochastic Burgers equation with a conserved, *uncorrelated* noise term, that is, the value of the noise at a given position and time and the values at surrounding positions and previous and following times present no statistical correlation. This assumption is an idealization of real physical systems, which generally exhibit both spatial and temporal correlations, at least in small scales [35]. Interestingly, the uncorrelated KPZ equation turns out to be a fairly good approximation to describe systems exhibiting short range correlations, given that the critical exponents are barely different from the uncorrelated case in these systems, as multiple studies have shown [1, 26]. Nonetheless, some relevant systems in the KPZ universality class can present long-range correlations, such as turbulent systems in the inertial range (spatial correlations) [39] or self-gravitating Newtonian fluids in the study of the matter distribution in the Universe (temporal correlations) [5]. In addition to modelling these systems, a study of the KPZ equation with long-range correlations provides a description of the transition from the uncorrelated (or weakly correlated) to the strongly correlated regime, suggesting the existence of a threshold correlation scale above which the critical exponents change drastically, as we shall see next.

The effects of long range correlations in the KPZ equation were first studied by E. Medina *et al.* [26], who proposed a description by means of the following noise correlator in the Fourier space (again considering just the one-dimensional case):

$$\langle \hat{\eta}(k, \omega) \hat{\eta}(k', \omega') \rangle \propto k^{-2\rho} \omega^{-2\theta}, \quad (4.1)$$

where  $\rho, \theta \in [0, 1/2)$  are quantifiers of the spatial and temporal correlations, respectively. The system behaves as an uncorrelated system when  $\rho = \theta = 0$ . Given the absence of an intrinsic length scale in the problem, several correlation functions yield the above expression in the limit of low frequencies in Fourier space, for instance

$$\langle \eta(x, t) \eta(x', t') \rangle = 2|x - x'|^{2\rho-1} |t - t'|^{2\theta-1}. \quad (4.2)$$

Multiple studies have addressed the case of the KPZ equation with spatially correlated noise, i.e. taking the limit  $\theta \rightarrow 0$  in eq. (4.2). The work by Medina *et al.* [26] itself included a renormalization group analysis for determining the critical exponents for  $\rho > 0$ , observing two distinguished regimes. Indeed, for correlations below a certain threshold  $\rho_c$ , they recovered the short-range ( $\rho = 0$ ) critical exponents, proving that the KPZ equation with uncorrelated noise is a good approximation in these cases. Above this limit, they found the following expressions for the critical exponents

$$z(\rho) = \frac{3 - 2\rho}{3}, \quad \alpha(\rho) = \frac{3 + 2\rho}{3}. \quad (4.3)$$

We notice that the Galilean invariance still holds, as  $\alpha(\rho) + z(\rho) = 2$  for all  $\rho$ . Later analytical and numerical studies have supported these results, for instance [21] and [28], to cite one of each.

In contrast, as already pointed out by Medina *et al.* [26], the case of temporally correlated noise is more complex, and literature on this problem has remained more

uncommon. Their work suggested the presence of two regimes separated by a threshold value  $\theta_c = 1/6$ , with the exponents remaining similar to the uncorrelated case for  $\theta < \theta_c$ . However, they realized that the Galilean invariance of the system is lost above the threshold, meaning that simple relations for the critical exponents like (4.3) cannot be found. Moreover, it has been recently shown [1, 35] that the Family-Vicsek scaling relation does not describe the system anymore as anomalous scaling emerges, whose features had already been described by J. J. Ramasco *et al.* [30] as we detailed in Chapter 1.

After getting the expected results when applying our integration scheme to the deterministic equation and the stochastic Burgers equation with white noise, our goal now is to study long-term temporally correlated noise, in order to obtain a new set of numerical values for the critical exponents in the range  $\theta \in (0, 1/2)$  that can be compared with previously published results. Before presenting our simulations, we carry out a brief overview of the recent analytical and numerical studies on this topic.

## 4.1 Existing results on long range temporal correlations

We start by considering two limit models for which the critical exponents are known and give some hints about the KPZ equation with temporally correlated noise. As we did in Chapter 3, we first study the linear case ( $\lambda = 0$ ), for which the exact critical exponents in terms of  $\theta$  can be derived. Next, we present the results of studies which addressed the limit  $\theta = 1/2$  by considering *columnar* noise (i.e. constant in time,  $\eta(x, t) \equiv \eta(x)$ ). This should give us an idea on how the system behaves under very strong correlations, in contrast with the analysis carried out Chapter 3 corresponding to the case  $\theta = 0$ . We will then aim at obtaining values in the intermediate region between these limit cases.

### 4.1.1 Edwards-Wilkinson equation with correlated noise

In their celebrated work, Medina *et al.* already gave the expression for the dependence of the critical exponents on the correlation quantifiers, based on simple dimensional analysis, even though their reasoning imposed a restriction on the dimension of the system and could not particularly be applied to  $d = 1$  [26]. Later approaches confirmed the validity of the relation in any dimension, which reads for  $d = 1$

$$z(\rho, \theta) \equiv 2, \quad \alpha(\rho, \theta) = 1/2 + \rho + 2\theta. \quad (4.4)$$

In particular, in the absence of spatially correlated noise, we expect  $\alpha(\theta) = 1/2 + \theta$ .

Nevertheless, anomalous scaling had not been suggested in the first studies on long range correlations, and it emerged both analytically and numerically in the work carried out by A. Alés and J. M. López [2]. Specifically, they identified super-roughness, by noticing that the roughness exponent of the velocity field  $u = \partial_x h$  becomes positive when  $\rho + 2\theta = 1/2$ . This leads to a rough velocity field and a separation of the so-called local roughness exponent and the global exponent  $\alpha$  at this threshold, which is found at  $\theta_c = 1/4$  if  $\rho = 0$ . We omitted the details of this kind of anomalous scaling since we shall focus on studying intrinsic anomalous scaling in KPZ. However, we highlight the existence of a threshold marking two regions with different scaling relations, which we will find again when studying the KPZ equation.

### 4.1.2 KPZ equation with columnar noise

The KPZ equation with columnar noise models a system for which the noise term takes a fixed value at each position for all times, while being uncorrelated from site to site. In other words, the differential equation ruling the process is

$$\partial_t h = \partial_x^2 h + \frac{\lambda}{2} (\partial_x h)^2 + \eta(x), \quad (4.5)$$

where  $\eta$  satisfies the correlation relation

$$\langle \eta(x)\eta(x') \rangle = 2\delta(x - x'). \quad (4.6)$$

This problem has major relevance on its own as it can be directly mapped, by performing the Cole-Hopf transformation from Chapter 2 backwards, to the diffusion equation of a classical field  $\Phi$  in the presence of random spatially distributed traps and sources [36]. Regarding our problem, columnar noise is equivalent to setting  $\theta = 1/2$  in eq. (4.2) and thus considering independence of the correlator on time. We should then expect the values of the critical exponents to approach the ones from eq. (4.5) as  $\theta$  grows towards  $1/2$ .

I. G. Szendro *et al.* carried out a numerical integration of eq. (4.5) and observed the formation of facets in the resulting interface, due to the exponential profile of the field  $\Phi$  around localization centers, which transforms into a straight line under the Cole-Hopf transformation [36]. Noticeably, the KPZ with columnar noise also showed anomalous scaling induced by the faceted pattern. In this case, the authors measured the values  $\alpha = 1.07 \pm 0.05$  and  $\alpha_s = 1.5 \pm 0.05$  for the global and spectral roughness exponents, respectively, showing that this kind of systems exhibits intrinsic anomalous scaling. In addition, they obtained  $z = 1.15 \pm 0.05$ . The results were in perfect agreement with the previous theoretical predictions [27, 30].

### 4.1.3 KPZ equation with correlated noise

The effects of long term correlations in the complete KPZ equation should describe the evolution of the critical exponents in the range between the limit values  $\theta = 0$  and  $\theta = 1/2$  that have already been discussed. However, while the dependence  $\alpha(\theta)$  is linear in the EW model, a different evolution is expected in KPZ as the critical exponents remain essentially for small correlations.

As discussed above, the behaviour below the threshold  $\theta_c = 1/6$  was described in the ground-breaking work of Medina *et al.* [26], who furthermore suggested the approximation

$$\alpha(\theta) = \frac{1 + 4\theta}{3 + 2\theta}, \quad z(\theta) = 2 - \alpha(\theta) \quad (4.7)$$

for  $\theta$  close above that point by neglecting the effects of the violation of Galilean invariance, and the relations

$$\alpha(\theta) = 1.69\theta + 0.22, \quad z(\theta) = \frac{2\alpha(\theta) + 1}{1 + 2\theta} \quad (4.8)$$

for  $\theta \in (\theta_c, 1/2)$ , obtained by solving numerically the flow equations given by DRG approach. Different analytical techniques have been developed since in order to estimate

the evolution of critical exponents, but the results do not perfectly agree with each other, some suggesting a different scenario with a smooth dependence on  $\theta$  and no threshold, such as the self-consistent expansion (SCE) developed by E. Kaztav and M. Schwartz [21]. In the quest of clarifying the issue, a recent work by D. Squizzato and L. Canet [35] carries out a non-perturbative renormalization group approach which supports the existence of a threshold value  $\theta_c$ .

On the numerical side, one of the most successful attempts can be found in the work by A. Alés and J. M. López [1]. They simulated both the KPZ equation and the ballistic deposition model, which lies within the KPZ universality class in the absence of correlation, with correlated noise for multiple  $\theta \in (0, 1/2)$ . Interestingly, their results show a smooth dependence  $\alpha(\theta)$ , but a different threshold index  $\theta_{\text{th}} \simeq 0.25$  does also play a role as it marks the point where intrinsic anomalous scaling begins to be noticed, in accordance with the predictions in the  $\theta \rightarrow 1/2$  limit following the study of the KPZ equation with columnar noise. Additionally, they observed the formation of faceted patterns in the height profile above a similar threshold, which was also spotted in the columnar noise limit. While none of these phenomena had been predicted by DRG techniques in the past, Squizzato and Canet obtained analytical results leading to a similar dependence on  $\theta$  of the difference  $\alpha - \alpha_s$  in [35].

Another unanswered question on this topic is whether the KPZ universality class is preserved when long term temporal correlations are considered, that is, whether systems within the KPZ universality class exhibit the same critical exponents as the KPZ model for large  $\theta$ . Our numerical simulations of the Burgers equation will help elucidate this matter, by directly comparing our results with the integration of the KPZ equation performed in [1]. Moreover, if the answer is positive, we will provide another set of values of the critical exponents for several  $\theta$ , increasing the statistical relevance of the numerical data describing the dependence  $\alpha(z)$ .

## 4.2 Numerical integration of the stochastic equation with correlated noise

The numerical analysis of the Burgers equation with correlated noise that we present here is not as complete as some of the aforementioned published works, since correctly measuring the critical exponents for a representative set of  $\theta$  would have required more time than available. There is still work in progress as this project extends beyond the results shown here and we expect to obtain significant data in the coming future.

Nonetheless, we were able to compute the critical exponents for a set of nine equally spread  $\theta \in (0, 0.5)$ . The relatively low statistical significance of our data do not let us assure the wished accuracy in the results, especially for large  $\theta$ , but they serve as approximations allowing to discuss the behaviour of correlated systems. In turn, we study in detail the cases  $\theta = 0.20$  and  $\theta = 0.45$ , which show the characteristic behaviour of each of the two regions separated by the threshold  $\theta_c$ , that we find to be around 0.25.

We use once again the discretization described in Section 1.3 and a flat initial condition. One of the effects of correlations below the threshold is delaying the entrance of the system in the asymptotic KPZ regime, therefore we set  $\lambda = 8$  throughout this section in order to ensure that we observe non-linear features. The numerical

integration followed the numerical scheme in Section 1.3, the correlated noise being generated through the method explained in Section 1.3.2. As a consequence of the introduction of correlated noise and large non-linearity, the numerical stability was compromised, and a larger  $\Delta t = 10^{-3}$  is used. Just as in Chapter 3, the relevant statistical observables corresponding to both fields  $u(x, t)$  and its primitive  $h(x, t)$  are measured.

We start by considering the system  $\theta = 0.20$ . Fig. 4.1 shows the time evolution of the surface roughness for systems of multiple sizes. Given that we now expect different roughness exponents in the EW and the KPZ regimes, we focus on sizes  $L \geq 512$ . This is because saturation in smaller sizes takes place earlier and the system does not clearly enter the KPZ regime before saturating, as we wish in order to measure the correct critical exponents. Likewise, we measure the growth exponent  $\beta$  only in the asymptotic region. Nonetheless, we observe again the presence of a first random deposition stage followed by the dominance of the linear regime, which grows at a rate compatible with the predicted  $\beta = \alpha(\theta)/z = 0.45$  for  $\theta = 0.20$  according to eq. (4.4). The slope in the asymptotic region stabilizes at  $\beta = 0.31$ . Regarding the roughness exponent, we measure  $\alpha = 0.51 \pm 0.03$  with larger uncertainty than in the uncorrelated case because less sizes can be considered now.

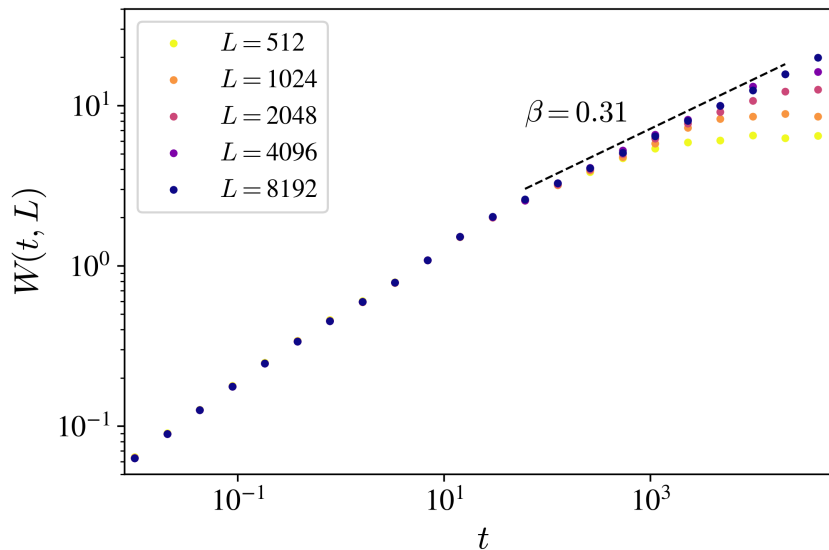


Figure 4.1: Time evolution of the surface roughness  $W(L, t)$  for systems of different lateral sizes with  $\theta = 0.20$ . The dashed line shows the linear fit in the asymptotic KPZ regime. A logarithmic scale is used in both axes.

As we see, for  $\theta = 0.20$  the main critical exponents are not noticeably different from the ones we measured in Chapter 3. The analysis of the PSD shown in Fig. 4.2 is consistent with these results. Using the same technique as in Section 3.3, we measure  $\alpha_s = 0.49 \pm 0.04$ , meaning that the global and the spectral roughness exponents are the same within the margin of uncertainty. This is confirmed as the upper part of the collapsed curves in the inset, which has slope  $\alpha - \alpha_s$  according to eq. (1.17), is essentially horizontal. Thus, for this correlation strength the system belongs to the Family-Vicsek class just as the uncorrelated systems. We later discuss the results obtained

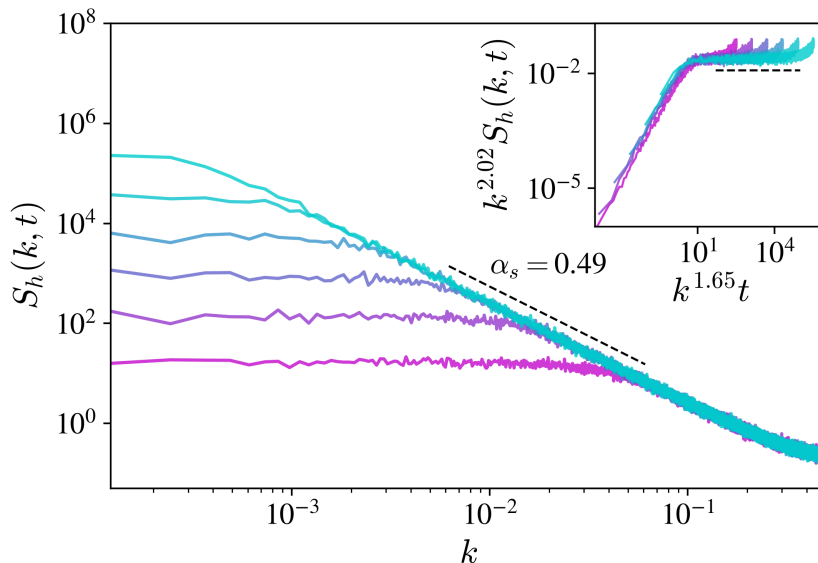


Figure 4.2: Power spectral density  $S_h(k, t)$  of the height field for  $L = 8192$  and  $\theta = 0.20$ . Starting at  $t_0 = 10.24$  (purple), each curve represents the PSD for a time 4 times greater than the one below. The inset shows the collapsed data using the exponents measured from the roughness evolution, leading to  $z = 1.65$  and  $2\alpha + 1 = 2.02$ .

for different  $\theta$ , which show a similar behaviour for  $\theta \leq 0.20$ , with  $\alpha \approx \alpha_s \approx 0.50$ , as Fig. 4.5 (left panel) shows.

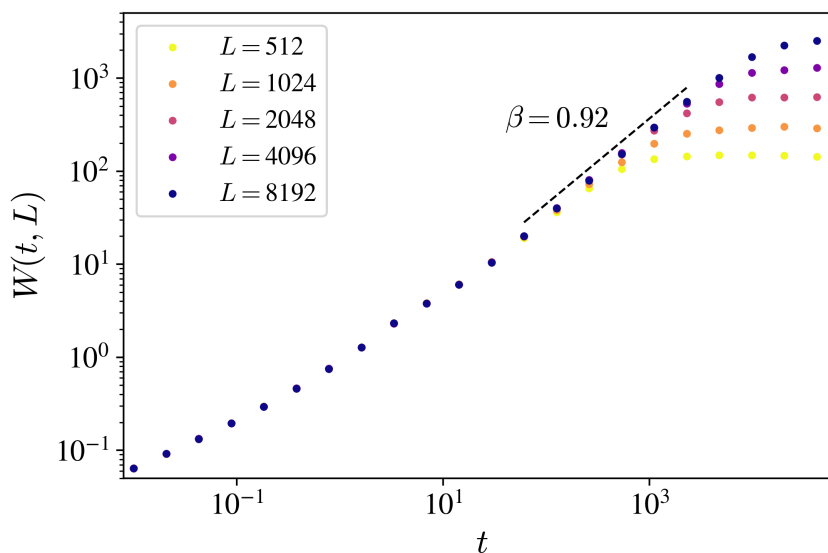


Figure 4.3: Time evolution of the surface roughness  $W(L, t)$  for systems of different lateral sizes with  $\theta = 0.45$ . The dashed line shows the linear fit in the asymptotic KPZ regime. A logarithmic scale is used in both axes.

In contrast, different results are observed when correlations are strong. The evolution of the surface roughness for  $\theta = 0.45$  is depicted in Fig. 4.3. Once again, the slope goes through different values marking the multiple regimes in the evolution of

the system, being compatible with the expected values  $\beta = 1/2$  and  $\beta = 0.70$  respectively in the random deposition and EW regimes. The slope in the asymptotic region is  $\beta = 0.92$ . In turn, we measure the global roughness exponent  $\alpha = 1.05 \pm 0.03$ .

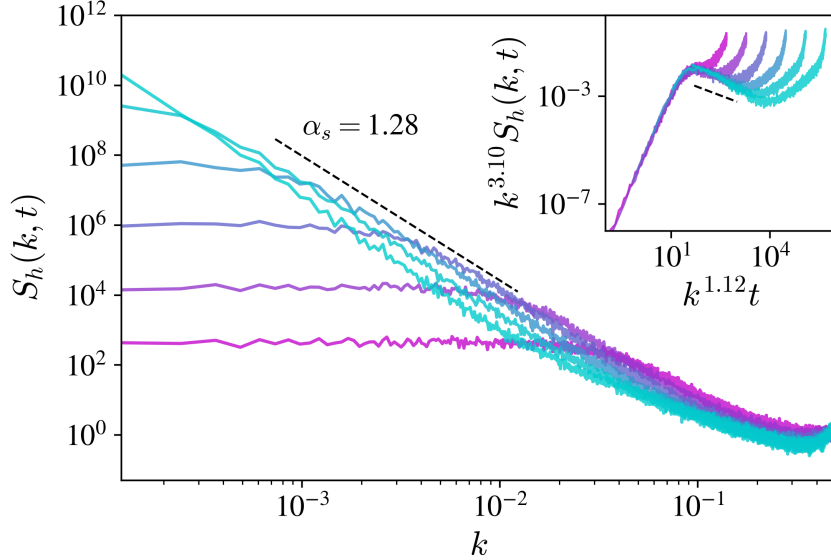


Figure 4.4: Power spectral density  $S_h(k, t)$  of the height field for  $L = 8192$  and  $\theta = 0.45$ . Starting at  $t_0 = 10.24$  (purple), each curve represents the PSD for a time 4 times greater than the one below. The inset shows the collapsed data using the exponents measured from the roughness evolution, leading to  $z = 1.12$  and  $2\alpha + 1 = 3.10$

The power spectral density of the height field in the  $L = 8192$  system is shown in Fig. 4.4. In this case, the aspect of  $S_h(k, t)$  for different times radically differs from the standard behaviour in kinetic roughening from Fig. 4.2, as the curves shift with time for large  $k$ . The spectral exponent is measured over the curve with longest time, yielding  $\alpha_s = 1.28 \pm 0.06$ . Thus, we obtain different values for the global and the spectral roughness exponent, meaning that intrinsic anomalous scaling rules the system. This is also seen in the inset, which depicts the collapsed data using  $\alpha = 1.05$ . Following eq. (1.17), the non-zero slope at large  $k^z t$  shows that  $\alpha \neq \alpha_s$ .

Thus, the obtained results in the two selected systems, with  $\theta = 0.20$  and  $\theta = 0.45$ , are fairly in accordance with the ones expected: the first system belongs to the Family-Vicsek scaling class but the second one does not, as intrinsic anomalous scaling is observed. Likewise, the critical exponents in the first case are similar to those from the uncorrelated KPZ equation, while great differences are observed for  $\theta = 0.45$ .

The analysis of the critical exponents over the range  $\theta \in [0, 0.5)$  is depicted in Fig. 4.5. For each correlation index  $\theta$ , we followed a similar procedure as in the two cases above: the growth exponent  $\beta$  and the global roughness exponent  $\alpha$  were measured from the time evolution of the surface roughness, while the spectral exponent was measured independently from the PSD of the largest size  $L = 8192$  in each case. The dynamic exponent was computed as  $z = \alpha/\beta$ .

Our results suggest the existence of a threshold index  $\theta_c \simeq 0.25$ . Below this value, the critical exponents vary very slowly with  $\theta$  from the ones of KPZ with uncorrelated noise. This behaviour is in accordance with the renormalization group

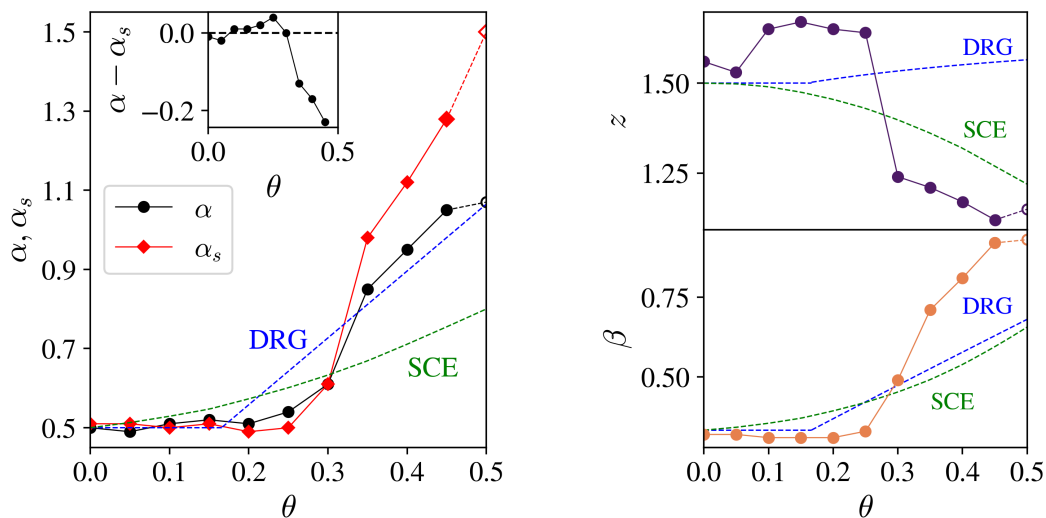


Figure 4.5: Global  $\alpha$  and spectral  $\alpha_s$  roughness exponents (left panel) and dynamic  $z$  and growth  $\beta$  exponents (right panel) for the different correlation indices  $\theta$  considered, including the data from Chapter 3 for  $\theta = 0$ . We show as well the dependencies predicted using DRG [26] and SCE [21], whereas the inset shows the difference  $\alpha - \alpha_s$ . In all cases, the critical exponents of KPZ with columnar noise [36] are shown at  $\theta = 0.5$  in order to display the expected limit.

analyses performed in [26] and [35], however the value that we get is noticeably larger than their  $\theta_c = 1/6$ . Various explanations can be given for this disagreement. On the one hand, the renormalization group approach is an approximation based on a perturbative series expansion. Hence, this technique does not necessarily provide a fully correct description of real systems. On the other hand, the detailed analysis of the case  $\theta = 0.30$ , not shown in this work, can also give a hint on the issue. The study of the surface roughness using this correlation index shows that small systems still belong to the Family-Vicsek scaling class, whereas large systems already exhibit features corresponding to strong correlations. This suggests that the threshold index depends to some extent on the lateral size  $L$ , and therefore it is reasonable that the finite systems that we simulated present a different threshold when compared with the ideal solutions derived by means of renormalization group techniques in the infinite size limit.

Conversely, some of our results are different from those observed in [1], which describe smooth increasing functions  $\alpha(\theta) = \alpha_s(\theta)$  for small  $\theta$ , yielding for instance  $\alpha \simeq 0.6$  for  $\theta = 0.20$ . This value does not lie within our uncertainty region for that correlation index. Likewise, similar accuracies in our results for  $\theta < 0.25$  lead to conclude that our results below this threshold disagree with the ones obtained in [1] by integrating the KPZ equation. This difference possibly comes from the fact that the integration method used in that work involves an approximation in order to ensure numerical stability, while our discretization scheme does not. These issues need to be explored further.

Due to longer saturation times and noisier PSD curves, the points with  $\theta > 0.25$  present larger uncertainties than the ones below the threshold, especially in the range  $[0.3, 0.4]$ . Despite that, the trend observed in this region is again in accordance with

previously published results. Our results show the splitting of the exponents  $\alpha$  and  $\alpha_s$  suggested in [1] and later supported by [35]. A raw analysis of the inset in Fig. 4.5 would set a threshold  $\theta_{\text{th}} \simeq 0.30$ , again slightly shifted with respect to the previously published result  $\theta_{\text{th}} \simeq 0.25$ . Nevertheless, the strong fluctuations in our data do not allow to confirm this disagreement. Faceted patterns have been observed as well above  $\theta_{\text{th}}$ , as Fig. 4.6 depicts.

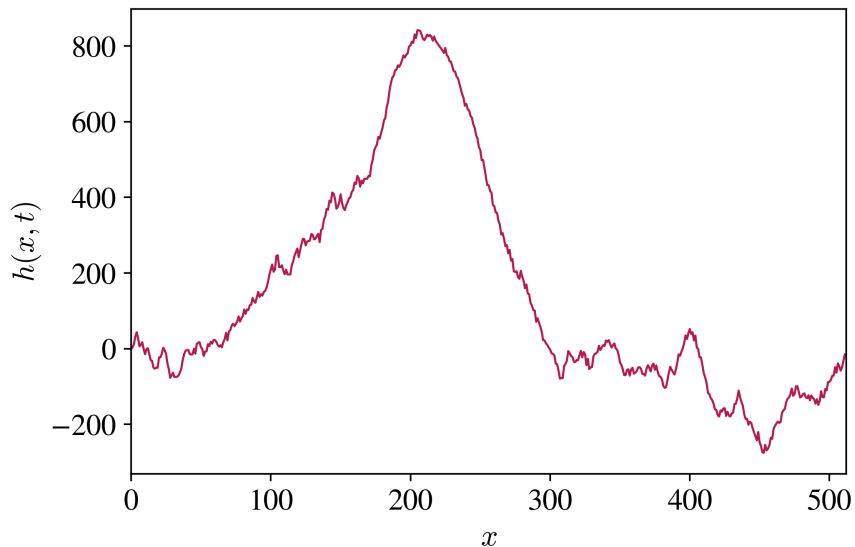


Figure 4.6: Snapshot of the height field at  $t = 5 \cdot 10^3$  in the  $L = 512$  system with  $\theta = 0.45$ , showing the formation of faceted patterns above  $\theta_{\text{th}}$ .

Furthermore, the points corresponding to the roughness exponent  $\alpha$  seem to match the prediction of the DRG analysis in [26] for  $\theta \geq 0.35$ , but this is not the case with the exponent  $z$  (and therefore the dependent  $\beta$ ). Previous studies [21, 35] have already shown this disagreement, proving the limitations of the DRG approach. Actually, we can see that the DRG prediction does not even agree with the expected columnar noise limit for these two exponents, while smooth prolongation of our results reach those values in all cases. Even more troublesome is the fact that existing renormalization group approaches do not even contemplate the existence of faceted patterns. Likewise, the SCE approximation provides a closer description of the dynamic exponent  $z$ , but lies considerably far from our data in the cases of  $\alpha$  and  $\beta$ , especially in the region close to  $\theta = 1/2$ . In turn, our simulations do not allow though to manifestly detect the breakdown of Galilean invariance, since the fluctuations of our measurements are comparable to the magnitude  $\alpha + z - 2$  after breaking.

## 5 Conclusions

In this work we carried out a numerical study of the one-dimensional stochastic Burgers equation as a model describing surface dynamics out of equilibrium. Indeed, the stochastic Burgers equation with conserved noise results from taking the spatial derivative in the celebrated KPZ equation, one of the paradigmatic models in non-equilibrium physics. Specifically, we were keen on analysing the effects of long-range temporally correlated noise on the Kardar-Parisi-Zhang equation. With this aim, we first integrated simpler versions of the problem, starting with the deterministic Burgers equation in Chapter 2 and following with the stochastic Burgers equation with uncorrelated noise in Chapter 3. These instances allowed us to check the integration method and refine the measurements that we wished to perform in Chapter 4, which addresses the case of temporally correlated noise.

The deterministic Burgers equation that we studied in Chapter 2 is an approximation of the Navier-Stokes equation, and thus is mostly used in the study of fluids. We were able to identify the main characteristics of this model and understand their relation with initial conditions and viscosity. Specifically, we observed the formation of shocks when the so-called characteristic lines cross each other, leading to a decay law in the effective energy. Our numerical scheme proved to be fairly stable for this equation, showing some sharp edges in the low viscosity case as a result of the emergence of shocks.

Our next step was to consider the stochastic Burgers equation with conserved, uncorrelated noise in Chapter 3. We integrated the equation in order to get the velocity field  $u(x, t)$  and then the primitive field  $h(x, t)$ , so that our results can be compared to the direct integration of the KPZ equation on the field  $h$ . Our simulations show the well-known features of systems within the KPZ universality class. The time evolution of the surface roughness exhibits the shape expected by the general theory of kinetic roughening. We detected that systems of different lateral sizes visit the random deposition and the Edwards-Wilkinson regimes before reaching the asymptotic KPZ state. Actually, the measured critical exponents show that the systems that we simulated saturate before fully leaving the linear EW regime. Longer computational times would have allowed us to consider larger sizes and thus better identify the asymptotic behaviour. The analysis of the PSD showed that the global and spectral roughness exponents coincide, in agreement with the Family-Vicsek scaling relation. Moreover, we saw that the probability distribution of the height field is up-down asymmetric during the asymptotic growing regime, as it follows the Tracy-Widom distribution, and then becomes symmetric in the saturation phase.

Lastly, Chapter 4 was dedicated to extending the integration method to the stochastic Burgers equation with long-range correlated noise, with the main goal of studying how the critical exponents evolve as temporal correlations become stronger. In this way, we numerically integrated the stochastic Burgers equation with correlated noise for a range of correlation indices  $\theta$  equally spaced in the range  $(0, 0.5)$ . We showed the existence of a threshold index  $\theta_c$  that marks a drastic change in the critical exponents of the correlated systems. Indeed, below  $\theta_c$  we find that critical exponents are essentially the same as in the uncorrelated case, while notably different values are obtained above  $\theta_c$ . In addition, we observed the emergence of intrinsic anomalous scaling at an

apparently different threshold index  $\theta_{\text{th}}$ , meaning that the solutions do not belong to the Family-Vicsek class anymore above that point. The results for strong correlations are consistent with the expected values in the limit  $\theta = 1/2$  corresponding to the KPZ equation with columnar noise.

Overall, our results provide a good description of the problem. They coincide with previously published studies on the problem in most qualitative features, while they agree only partially in quantitative aspects, some values showing a noticeable disagreement with the existing predictions. Future work under this approach should focus on obtaining more accurate values for the critical exponents and measuring them over a denser set of  $\theta$ , namely giving a detailed description of the dependence close to the thresholds  $\theta_c$  and  $\theta_{\text{th}}$ . This would also allow to determine whether their values are the same or not, since the precision of our results is not enough to resolve this. Furthermore, we remind that there are very few aspects in which all the existing literature on the problem agrees. Given the lack of an exact solution, analytical studies rely on different approximations that manage to describe some of the observed features but fail in others. For this reason, there is still a lot to be done in the understanding of the effects of temporally correlated noise in the KPZ equation.

The results shown here are part of a project that extends beyond this work and aims at simulating other correlated equations whose uncorrelated versions lie within the KPZ universality class, such as the ballistic deposition model or directed polymers in random media. In this way, we head towards the ultimate goal of comparing the data collected from the different systems and shedding some light on this problem.

## References

- [1] ALÉS A., LÓPEZ J. M. (2019), “Faceted patterns and anomalous surface roughening driven by long-range temporally correlated noise”, *Phys. Rev. E* **99**, 062139.
- [2] ALÉS A., LÓPEZ J. M. (2020), “Surface super-roughening driven by spatiotemporally correlated noise”, *J. Stat. Mech.: Theory Exp.*, 033210.
- [3] AMIR G., CORWIN I., QUASTEL J. (2011), “Probability Distribution of the Free Energy of the Continuum Directed Random Polymer in 1 + 1 dimensions”, *Comm. Pure Appl. Math.* **64**, 466-537.
- [4] BARABÁSI A.-L., STANLEY H. E. (1995), *Fractal Concepts in Surface Growth*, Cambridge University Press.
- [5] BARBERO J. F., DOMÍNGUEZ A., GOLDMAN T. et al. (1997), “Dynamical critical phenomena and large-scale structure of the Universe: The power spectrum for density fluctuations”, *Europhys. Lett.* **38**, 637.
- [6] BATEMAN H. (1915), “Some recent researches on the motion of fluids”, *Mon. Weather Rev.* **43** (4), 163-170.
- [7] BONKILE M. P., AWASTHI A., LAKSHMI C. et al. (2018), “A systematic literature review of Burgers’ equation with recent advances”, *Pramana - J. Phys* **90**, 69.
- [8] BURGERS J. M. (1948), “A Mathematical Model Illustrating the Theory of Turbulence”, *Adv. Appl. Math.* **1**, 171-199.
- [9] CANET L., CHATÉ H., DELAMOTTE B. et al. (2012), “Nonperturbative renormalization group for the Kardar-Parisi-Zhang equation: general framework and first applications”, *Phys. Rev. E* **84**, 061128.
- [10] CORWIN I. (2011), “The Kardar-Parisi-Zhang equation and universality class”, *Random Matrices: Theo. Appl.* **1**, 1130001.
- [11] CRAIG W. (2018), *A course on Partial Differential Equations*, American Mathematical Society.
- [12] EDWARDS S. F., WILKINSON D. R. (1982), “The Surface Statistics of a Granular Aggregate”, *Proc. R. Soc. London A* **381**, 17-31.
- [13] ERTAŞ D., KARDAR M. (1993), “Dynamic relaxation of drifting polymers: A phenomenological approach”, *Phys. Rev. E* **48** (2), 1228-1245.
- [14] FAMILY F., VICSEK T. (1985), “Scaling of the active zone in the Eden process on percolation networks and the ballistic deposition model”, *J. Phys. A* **18**, L75-L81.
- [15] FRISCH U. (1995), *Turbulence*, Cambridge University Press.
- [16] FRISCH U., BEC J. (2000), “Burgulence”, *New trends in turbulence. Turbulence: nouveaux aspects*, Springer Verlag.

- [17] Y. C. HON, H. Z. MAO (1998), “An efficient numerical scheme for Burgers equation”, *App. Math. Comput.* **95** (1), 37-50.
- [18] INOUE A. (1994), “Tauberian Theorems for Fourier Cosine Transforms”, *Hokkaido University Preprint Series in Mathematics* **249**, 1-9.
- [19] JOHANSSON T. (2000), “Shape fluctuations and random matrices”, *Commun. Math. Phys.* **209** (2), 437-476.
- [20] KARDAR M., PARISI G., ZHANG Y.-C. (1986), “Dynamic Scaling of Growing Interfaces”, *Phys. Rev. Lett.* **56**, 889.
- [21] KAZTAV E., SCHWARTZ M. (1999), “Self-consistent expansion for the Kardar-Parisi-Zhang equation with correlated noise”, *Phys. Rev. E* **60**, 5677.
- [22] KRIECHERBAUER T., KRUG J. (2010). “A pedestrian’s view on interacting particle systems, KPZ universality and random matrices”, *J. Phys. A: Math. Theor.* **43**, 403001.
- [23] LUI T. P. (2017), “Hopf-Cole transformation”, *B. Inst. Math. Acad. Sinica* **12** (1), 71-101.
- [24] MANDELBROT B. B. (1971), “A Fast Fractional Gaussian Noise Generator”, *Water Resour. Res.* **7** (3), 543-553.
- [25] MOREIRA J. G., DA SILVA J. K. L., KAMPHORST S. O. (1994), “On the fractal dimension of self-affine profiles”, *J. Phys. Math. Gen.* **27**, 8079.
- [26] MEDINA E., HWA T., KARDAR M. et al. (1989), “Burgers equation with correlated noise: Renormalization-group analysis and applications to directed polymers and interface growth”, *Phys. Rev. A* **39**, 3053.
- [27] NATTERMANN T., RENZ W. (1989), “Diffusion in a random catalytic environment, polymers in random media, and stochastically growing interfaces”, *Phys. Rev. A* **40**, 4675.
- [28] PENG C.-K., HAVLIN S., SCHWARTZ M. et al. (1991), “Directed-polymer and ballistic-deposition growth with correlated noise”, *Phys. Rev. A* **44**, R2239.
- [29] QUASTEL J., SPOHN H. (2015), “The one-dimensional KPZ equation and its universality class”, *J. Stat. Phys.* **160** (4), 965-984.
- [30] RAMASCO J. J., LÓPEZ J. M., RODRÍGUEZ M. A. (2000), “Generic Dynamic Scaling in Kinetic Roughening”, *Phys. Rev. Letters* **84**, 10.
- [31] RODRÍGUEZ FERNÁNDEZ E. (2022), “Fluctuations and patterns in ultrathin fluid films”, Ph.D. Thesis, Universidad Carlos III de Madrid.
- [32] SARRA S. (2003), “The Method of Characteristics with applications to Conservation Laws”, *J. Online Math. Appl.* **3**.

- [33] SASAMOTO T., SPOHN H. (2009), “Superdiffusivity of the 1D Lattice Kardar-Parisi-Zhang Equation”, *J. Stat. Phys.* **137** (917).
- [34] SASAMOTO T., SPOHN H. (2010), “One-dimensional KPZ equation: an exact solution and its universality”, *Phys. Rev. Lett.* **104** (23).
- [35] SQUIZZATO D., CANET L. (2019), “Kardar-Parisi-Zhang equation with temporally correlated noise: A nonperturbative renormalization group approach”, *Phys. Rev. E* **100**, 062143.
- [36] SZENDRO I. G., LÓPEZ J. M., RODRÍGUEZ M. A. et al. (2007), “Localization in disordered media, anomalous roughening, and coarsening dynamics of faceted surfaces”, *Phys. Rev. E* **76**, 011603.
- [37] TRACY C. A., WIDOM H. (1994), “Level-spacing distributions and the Airy kernel”, *Comm. Math. Phys.* **159** (1), 151-174.
- [38] WOLCHOVER N. (2016), *At the Far Ends of a New Universal Law*, book chapter in *The Best Writing on Mathematics*, Princeton University Press.
- [39] YAKHOT V., ORSZAG S. A. (1986), “Renormalization-Group Analysis of Turbulence”, *Phys. Rev. Lett.* **57**, 1722.